

# Three-Dimensional Simulations of SASI- and Convection-Dominated Core-Collapse Supernovae

Rodrigo Fernández<sup>1,2</sup>

<sup>1</sup> *Department of Physics, University of California, Berkeley, CA 94720, USA*

<sup>2</sup> *Department of Astronomy & Theoretical Astrophysics Center, University of California, Berkeley, CA 94720, USA*

Submitted to MNRAS

## ABSTRACT

We investigate the effect of dimensionality on the transition to explosion in neutrino-driven core-collapse supernovae. Using parameterized hydrodynamic simulations of the stalled supernova shock in one-, two- (2D), and three spatial dimensions (3D), we systematically probe the extent to which hydrodynamic instabilities alone can tip the balance in favor of explosion. In particular, we focus on systems that are well into the regimes where the Standing Accretion Shock Instability (SASI) or neutrino-driven convection dominate the dynamics, and characterize the difference between them. We find that SASI-dominated models can explode with up to  $\sim 20\%$  lower neutrino luminosity in 3D than in 2D, with the magnitude of this difference decreasing with increasing resolution. This improvement in explosion conditions is related to the ability of spiral modes to generate more non-radial kinetic energy than a single sloshing mode, increasing the size of the average shock radius, and hence generating better conditions for the formation of large-scale, high-entropy bubbles. In contrast, convection-dominated explosions show a smaller difference in their critical heating rate between 2D and 3D ( $< 8\%$ ), in agreement with previous studies. The ability of our numerical implementation to maintain arbitrary symmetries is quantified with a set of SASI-based tests. We discuss implications for the diversity of explosion paths in a realistic supernova environment.

**Key words:** hydrodynamics – instabilities – neutrinos – nuclear reactions, nucleosynthesis, abundances – shock waves – supernovae: general

## 1 INTRODUCTION

While the explosion mechanism of massive stars is still an unsolved problem, important progress has been made in the last few decades on the theory side (see, e.g., Fogliizzo et al. 2015 for a recent review). At present, the leading explanation for the majority of core-collapse supernovae is the *neutrino mechanism*, in which energy deposition by a small fraction of the outgoing neutrinos powers the revival of the stalled shock (Bethe & Wilson 1985). State-of-the-art models have shown that this mechanism fails in spherical symmetry, except for a small fraction of progenitors at the low mass end for core-collapse (e.g., Janka 2012 and references therein).

Significant effort has been invested in the development of multi-dimensional hydrodynamic models, first in axisymmetry (2D; e.g. Herant et al. 1992; Burrows et al. 1995; Janka & Müller 1996; Ott et al. 2008; Suwa et al. 2010; Bruenn et al. 2013) and recently in three spatial dimensions (3D), with varying degrees of approximation for other physics such as neutrino transport (e.g., Hanke et al. 2013 and references therein). These stud-

ies and others have demonstrated the importance of hydrodynamic instabilities for providing favorable conditions for explosion. Observationally, an asymmetric explosion is expected from spectropolarimetry (e.g., Wang & Wheeler 2008), the distribution of elements in supernova remnants (e.g., Grefenstette et al. 2014), and the large proper motions of pulsars (e.g., Hobbs et al. 2005).

Two types of instability can break the symmetry of a stalled shock. First, neutrino energy deposition drives buoyant *convection* in a layer just inside the shock (e.g., Bethe 1990). This is a local instability that generates kinetic energy on relatively small spatial scales (spherical harmonic indices  $\ell \gtrsim 5$ ). Second, the shock is unstable to a global oscillatory instability driven by a cycle of advected and acoustic perturbations trapped in between the shock and the neutrinosphere: the Standing Accretion Shock Instability (SASI; Blondin et al. 2003; Blondin & Mezzacappa 2006; Fogliizzo et al. 2007; Guilet & Fogliizzo 2012). This instability favors larger spatial scales than convection ( $\ell \sim 1 - 2$ ). Non-axisymmetric (spiral) modes of the SASI can also lead

to angular momentum redistribution, as found in numerical simulations (Blondin & Mezzacappa 2007; Blondin & Shaw 2007; Fernández 2010; Guilet & Fernández 2014) and in experiments (Foglizzo et al. 2012).

The first generation of 2D supernova models with advanced neutrino transport found strong sloshing activity in the shock preceding explosion, and hence the SASI was generally credited for contributing to this success (e.g., Burrows et al. 2007; Marek & Janka 2009). But because the inverse cascade in 2D turbulence transfers kinetic energy to large spatial scales, it was not clear whether these sloshings were in fact driven by the SASI or just a consequence of convective activity (e.g., Fernández & Thompson 2009a). Thereafter, the first batch of 3D hydrodynamic core-collapse models with approximate neutrino physics did not yield prominent sloshings in exploding cases (Fryer & Young 2007; Nordhaus et al. 2010; Hanke et al. 2012; Takiwaki et al. 2012; Couch 2013; Dolence et al. 2013), showing instead all the signs of buoyant convection driving the dynamics (Burrows et al. 2012; Murphy et al. 2013). These early 3D studies however focused on a small set of progenitors.

The full-physics 2D study of Müller et al. (2012) collapsed two progenitors ( $8.1$  and  $27M_{\odot}$ ) with very different inner density profiles (compactness), and found two distinctive explosion paths: one dominated by convection and another dominated by the SASI at low and high accretion rates, respectively. A followup study of the  $27M_{\odot}$  progenitor in 3D using sophisticated neutrino transport found episodic SASI activity, but no successful explosion (Hanke et al. 2013). Other studies using more approximate transport did not find a dominant SASI in exploding systems (Ott et al. 2013; Couch & O’Connor 2014; Abdikamalov et al. 2014).

The presence of SASI activity leads to specific predictions regarding the neutrino signal (Marek et al. 2009; Lund et al. 2010, 2012; Tamborra et al. 2013, 2014) and gravitational wave emission (e.g., Murphy et al. 2009; Kotake et al. 2011; Müller et al. 2013). The differences introduced by dimensionality in *bona fide* SASI-dominated explosions have not been systematically explored yet, with the closest work being the parametric models of Hanke et al. (2013) and Iwakami et al. (2008, 2014), in which systems straddle both instability regimes (convection parameter close to the critical value) at the time when the shock stalls or in the initial condition. In contrast, multiple 3D studies have addressed convection-dominated systems, finding either relatively minor differences in the susceptibility to explosion between 2D and 3D (e.g., Hanke et al. 2012; Dolence et al. 2013; Handy et al. 2014), or more detrimental conditions in 3D (e.g., Hanke et al. 2013; Couch & O’Connor 2014; Mezzacappa et al. 2015; Lentz et al. 2015; although recent work by Müller 2015 suggests that 3D can be more favorable than 2D *after* the onset of explosion). A better understanding of SASI-dominated explosions is important within the search for a robust explosion mechanism, because the susceptibility to the SASI depends not only on the compactness of the progenitor via the accretion rate, but also on the speed at which the protoneutron star contracts (Scheck et al. 2008). Therefore, the current generation of models could be underestimating the prevalence of the SASI given the treatment of neutrino

physics and the uncertainties in the stellar models and equation of state (EOS).

Here we investigate the transition to explosion using parameterized hydrodynamic models that, while approximate, are free from uncertainties about the progenitor and the EOS, allowing a clean test of the hydrodynamic effects in 2D and 3D. Model parameters can be controlled so that at explosion, they lie well within the regime of dominance of either instability. Our approach builds on the study of Fernández et al. (2014, hereafter Paper I), who characterized the properties of SASI- and convection-dominated explosions in 2D. The main conclusion of that study is that both types of explosion succeed by generating large-scale, high-entropy bubbles in different ways: either directly via large-scale shock expansions (SASI) or through the dynamics of convective bubble growth. Our focus here is to probe the differences introduced by adding the 3rd spatial dimension to SASI-dominated systems, and to compare the outcome to convection-dominated explosions.

The structure of the paper is the following. Section 2 describes the physical model and numerical method used, and the list of models evolved. Section 3 presents our results, with an overview of the transition to explosion, the role of dimensionality and resolution, and the properties of non-exploding SASI-dominated systems. Section 4 summarizes our results and discusses the implications for our understanding of core-collapse supernovae. The Appendix describes the extension of the code to 3D and a set of SASI-based tests to quantify its accuracy.

## 2 METHODS

### 2.1 Physical Model and Initial Condition

In order to study the hydrodynamic instabilities that arise during the stalled shock phase of core-collapse supernovae, we employ a non-rotating spherical accretion flow with a standing shock as the baseline state. This solution assumes constant mass accretion rate, constant neutron star radius, and employs a gamma-law equation of state with parameterized charged-current neutrino source terms, including ‘light bulb’ irradiation. This type of model was first used by Blondin et al. (2003) without heating to isolate the SASI, and has been subsequently employed in a number of parametric studies of the CCSNe mechanism (Foglizzo et al. 2006, 2007; Fernández & Thompson 2009b,a; Guilet et al. 2010; Guilet & Foglizzo 2012).

This parametric approach has two advantages: (1) the results are independent of the uncertainties in stellar models, the dense matter EOS, or an incomplete treatment of neutrino transport; and (2) the linear stability properties of the system are well understood (Foglizzo et al. 2007; Fernández & Thompson 2009b), enabling the construction of model sequences in well-defined regions of parameter space. The resulting flow in the gain region compares favorably with models that include more physics (Paper I).

The initial condition consists of a steady-state spherical accretion flow incident on a neutron star of mass  $M_{\text{ns}}$  and radius  $r_*$ , with a standing shock at a radius  $r_s$ . The flow outside of the shock is adiabatic and supersonic, with Mach number  $\mathcal{M}_0$  at a fiducial radius  $r_0$ . Inside the shock

the flow is subsonic, decelerating onto the neutron star surface through the emission of neutrinos and geometric convergence. The specific rate of neutrino heating and cooling is parameterized as

$$Q_\nu = \left[ \frac{B}{r^2} - Ap^{3/2} \right] e^{-(s/s_{\min})^2} \Theta(\mathcal{M}_{\text{cut}} - \mathcal{M}), \quad (1)$$

where  $p$  is the pressure and  $s$  is the entropy. The minimum entropy  $s_{\min}$  prevents runaway cooling, while the cutoff Mach number  $\mathcal{M}_{\text{cut}}$  suppresses source terms in the upstream flow.

To generate a model sequence, we first fix the cooling normalization in the absence of heating ( $B = 0$ ). Given the ratio of shock to stellar radius  $r_s/r_*$ , with  $r_s = r_0$ , the adiabatic index  $\gamma$ , and the constant rate of nuclear dissociation at the shock  $\varepsilon$ , the cooling normalization  $A$  is found by requiring that the radial velocity vanishes at  $r = r_*$ . The sequence is then formed by varying the heating constant  $B$ , which is related to the lightbulb neutrino luminosity by

$$B \simeq 0.007 L_{\nu e,52} T_{\nu,4}^2 \left( \frac{r_0}{100 \text{ km}} \right)^{1/2} \left( \frac{1.3 M_\odot}{M_{\text{ns}}} \right)^{3/2}, \quad (2)$$

where  $L_{\nu e,52} = L_{\nu e}/(10^{52} \text{ erg s}^{-1})$  is the electron neutrino luminosity and  $T_{\nu,4} = T_\nu/(4 \text{ MeV})$  is the neutrinospheric temperature. Increasing  $B$  increases the initial shock radius  $r_s$  from its value without heating,  $r_0$ . The minimum entropy  $s_{\min}$  is obtained separately for each model, by computing the entropy at  $r = r_*$  without using the exponential cutoff in equation (1). The numerical value is obtained using the ideal gas entropy normalized to its post-shock value (e.g., Foglizzo et al. 2007)

$$s = \frac{1}{\gamma - 1} \ln \left[ \frac{p}{p_2} \left( \frac{\rho_2}{\rho} \right)^\gamma \right], \quad (3)$$

where  $\rho_2$  and  $p_2$  are the initial post-shock density and pressure. The initial condition for the time-dependent simulation is then obtained by re-computing the solution including the entropy cutoff  $s_{\min}$  in equation (1).

To connect with previous work, we employ an adiabatic index  $\gamma = 4/3$ , a ratio of shock to stellar radius without heating  $r_0/r_* = 0.4$ , and an upstream Mach number  $\mathcal{M}_0 = 5$ . Examples of the type of initial condition obtained with this model can be found in Fernández & Thompson (2009a). Throughout the paper, we make use of a general unit system that reflects the dimensionless character of the problem. These units and their characteristic values in the core-collapse supernova problem are described in Table 1.

## 2.2 Numerical Setup

We use FLASH3.2 (Fryxell et al. 2000; Dubey et al. 2009) to solve the Euler equations in spherical polar coordinates  $(r, \theta, \phi)$ , subject to the gravity of a point mass and neutrino energy source terms,

$$\frac{\partial \rho}{\partial t} + \nabla \cdot (\rho \mathbf{v}) = 0 \quad (4)$$

$$\frac{\partial \mathbf{v}}{\partial t} + (\mathbf{v} \cdot \nabla) \mathbf{v} = -\frac{1}{\rho} \nabla p - \frac{GM_{\text{ns}}}{r^2} \hat{r} \quad (5)$$

$$\frac{de_{\text{int}}}{dt} - \frac{p}{\rho^2} \frac{d\rho}{dt} = Q_\nu. \quad (6)$$

**Table 1.** Frequently-used quantities and reference values applicable to core-collapse supernovae. The use of a gamma-law equation of state and an arbitrary normalization for the cooling function allow a dimensionless formulation of the problem.

Symbol	Quantity	CCSN Reference value
$r_0$	Initial shock radius with $B = 0$	100 $r_{100}$ km
$B$	Heating amplitude	Equation (2)
$M_{\text{ns}}$	NS mass	1.3 $M_{1.3}$ $M_\odot$
$\dot{M}$	Accretion rate	0.2 $\dot{M}_{0.2}$ $M_\odot \text{ s}^{-1}$
$v_{\text{ff}}$	$(2GM_{\text{ns}}/r_0)^{1/2}$	$10^{9.77} M_{1.3}^{1/2} r_{100}^{-1/2}$ cm $\text{s}^{-1}$
$t_0$	$r_0/v_{\text{ff}}$	$1.7 r_{100}^{3/2} M_{1.3}^{-1/2}$ ms
$E_0$	$\dot{M} r_0 v_{\text{ff}}$	$10^{49.37} \dot{M}_{0.2} r_{100}^{1/2} M_{1.3}^{1/2}$ erg

where  $\rho$ ,  $\mathbf{v}$ ,  $e_{\text{int}}$  are the density, velocity, and internal energy, and  $d/dt = \partial/\partial t + \mathbf{v} \cdot \nabla$ . The system of equations is closed with an ideal gas equation of state, and the point mass  $M_{\text{ns}}$  remains constant in time.

The public version of FLASH has been modified to enable the split Piecewise Parabolic Method (PPM) solver to operate in 3D spherical coordinates. A detailed description of the changes to the code and verification tests of the implementation are presented in Appendix A. The code has previously been modified to enable use of a non-uniform grid, as described in Fernández (2012).

The computational domain covers the full range of polar angles,  $\theta \in [0, \pi]$  and  $\phi \in [0, 2\pi]$ . In the radial direction, the domain extends from  $r = r_* = 0.4r_0$  to  $r = 7r_0$ . The radial grid is logarithmically spaced with 640 cells, resulting in a constant fractional spacing  $\Delta r/r = 0.45\%$  or  $0.26^\circ$ . The meridional grid has constant spacing in  $\cos \theta$ , and the azimuthal grid is uniform. This angular spacing yields cells that subtend a constant solid angle at fixed radius.

We adopt two resolutions for the angular grid in order to test the sensitivity of the results to this variable. The baseline resolution employs 56 cells in the  $\theta$  direction and 192 cells in  $\phi$ , for an effective resolution  $\Delta \theta \simeq \Delta \phi \simeq 2^\circ$  at the equator. In addition, we evolve two models at twice the resolution in both  $\theta$  and  $\phi$  (112 and 384 grid points, respectively). Our radial resolution is among the highest in published 3D hydrodynamic supernova studies, while our baseline angular resolution is comparable to that of Hanke et al. (2013), Mezzacappa et al. (2015), and Melson et al. (2015b). Our highest angular resolution ( $1^\circ$  at the equator) is only a factor of 2 lower than the highest resolution of Burrows et al. (2012), Couch & O'Connor (2014), and Abdikamalov et al. (2014).

The boundary condition in azimuth is periodic. In the radial direction, we use a reflecting inner boundary at  $r = r_*$ , and set the ghost cells to the steady-state solution at the outer boundary. In the  $\theta$  direction, we fill the ghost cells with information from active cells located across the axis (Appendix A); for comparison, we also run a model with a reflecting boundary condition in  $\theta$ .

### 2.3 Models Evolved

We evolve two sequences of models, each with increasing heating rate  $B$  (eq. [2]), as shown in Table 2. The two sequences differ in the magnitude of the nuclear dissociation  $\varepsilon$  at the shock, which changes the strength of the shock jump and thus the magnitude of the postshock velocity (e.g., Thompson 2000). This difference places each sequence well above and below the bifurcation in parameter space that determines whether the SASI or convection dominate the dynamics.

The relative importance of each instability is set by the relation between the advection rate and convective growth rate in the initial condition. This can be quantified with the ‘convection’ parameter (Foglizzo et al. 2006)

$$\chi = \int_{r_g}^{r_s} \frac{|\omega_{\text{BV}}| dr}{|v_r|}, \quad (7)$$

where  $\omega_{\text{BV}}$  is the Brunt-Väisälä frequency, and the integral runs from the gain radius  $r_g$  to the shock radius  $r_s$ . The transition from SASI- to convection-dominance occurs around  $\chi \simeq 3$ . Our *SASI-dominated* sequence (models names starting with ‘s’) has  $\varepsilon = 0$ , yielding values of  $\chi \ll 3$  in all initial models, while the *convection-dominated* sequence (model names starting with ‘c’) has  $\varepsilon = 0.3GM_{\text{ns}}/r_0$ , yielding  $\chi \gg 3$  for all values of  $B$ .

For both sequences, we evolve models in 1D, 2D, and 3D around the critical value of  $B$  for which an explosion is obtained. For 1D and 2D, these critical values were obtained in Paper I. Here we recompute the same models to maintain consistency with 3D in the numerical implementation and grid resolution<sup>1</sup>. The critical heating rates for 1D and 2D models are consistent with the previous value.

Two types of initial perturbation are applied. In most cases, random velocity perturbations in all coordinate directions are applied over the entire computational domain at  $t = 0$ , with magnitude 0.1% of the radial velocity. In a few models, an overdense spherical shell with an  $\ell = 1$  angular dependence is added to the flow (as in, e.g., Blondin & Mezzacappa 2006 or Fernández & Thompson 2009b). The dipole axis of this perturbation is not aligned with any cartesian coordinate direction, pointing instead towards  $\theta = \phi = 45^\circ$ . This perturbation excites a clean sloshing SASI mode, thus imposing a deterministic initial condition for probing the effects of dimensionality and resolution. Appendix A shows how this type of perturbation is used as a test of the ability of the code to maintain different symmetries.

A model is considered to have exploded when the shock radius reaches or approaches the outer radial computational boundary. For the 1D case with finite nuclear dissociation, we assign an explosion time at the moment when the periodic oscillation cycle is broken. Explosion times are listed in Table 2. Most models are evolved up to a time  $t = 500t_0$  or until they explode, whichever comes first<sup>2</sup>.

<sup>1</sup> The models of Paper I did not employ a hybrid Riemann solver at the shock, whereas our 3D implementation requires such a hybrid approach to minimize numerical noise (Appendix A).

<sup>2</sup> The high-resolution model S08L1-hr is interrupted earlier than  $500t_0$  when it appears that it will not explode, to save computing time.

**Table 2.** Model parameters and explosion time. Columns show from left to right: model name, nuclear dissociation energy at the shock, heating normalization (eqns. [1]-[2]), initial  $\chi$  parameter (eq. [7]), type of perturbation ( $\delta\mathbf{v}$ : random velocity,  $\ell = 1$ : overdense shell), and explosion time. A model is considered to have exploded when the shock hits or approaches the outer simulation boundary. For 1D cases with  $\varepsilon \neq 0$ , the model ‘explodes’ when the shock oscillation is broken by transient expansion (e.g. model c1d-08).

Model	$\varepsilon$ ( $GM_{\text{ns}}/r_0$ )	$B$ ( $10^{-3}$ )	$\chi$	Pert.	$t_{\text{exp}}$ ( $t_0$ )
1D:					
s1d-09	0	9	1.3	...	...
s1d-10		10	1.6	...	...
s1d-11		11	1.8	...	314
c1d-07	0.3	7	9.1	...	...
c1d-08		8	11	...	350
2D:					
s2d-00	0	0	0	$\delta\mathbf{v}$	...
s2d-06		6	0.6		...
s2d-08		8	1.1	$\ell = 1$	...
s2d-09		9	1.3	$\delta\mathbf{v}$	...
s2d-09hr					...
s2d-10		10	1.6		238
s2d-10hr					256
c2d-06	0.3	6	7.1		...
c2d-06hr					...
c2d-065		6.5	8.0		...
c2d-065hr					...
c2d-07		7	9.1		423
c2d-07hr					339
3D:					
S00dv	0	0	0	$\delta\mathbf{v}$	...
S06dv		6	0.6		...
S07dv		7	0.8		...
S08dv		8	1.1		306
S09dv		9	1.3		204
S10dv		10	1.6		219
S08L1	0	8	1.1	$\ell = 1$	172
S08L1-ref					270
S08L1-hr					...
S09dv-hr		9	1.3	$\delta\mathbf{v}$	187
C06dv	0.3	6	7.1	$\delta\mathbf{v}$	...
C065dv		7	8.0		...
C07dv		7	9.1		336
C07dv-hr					313

## 3 RESULTS

### 3.1 Transition to Explosion: Overview

To illustrate the general behavior of SASI-dominated systems, we describe the evolution of the marginally-exploding 3D model S08dv (Table 2). Initially, a dominant sloshing SASI mode grows out of random initial velocity perturbations, as shown in Figure 1a. As this mode achieves saturation, sloshing modes in orthogonal directions also grow and become non-linear, slightly out-of-phase, but the resulting

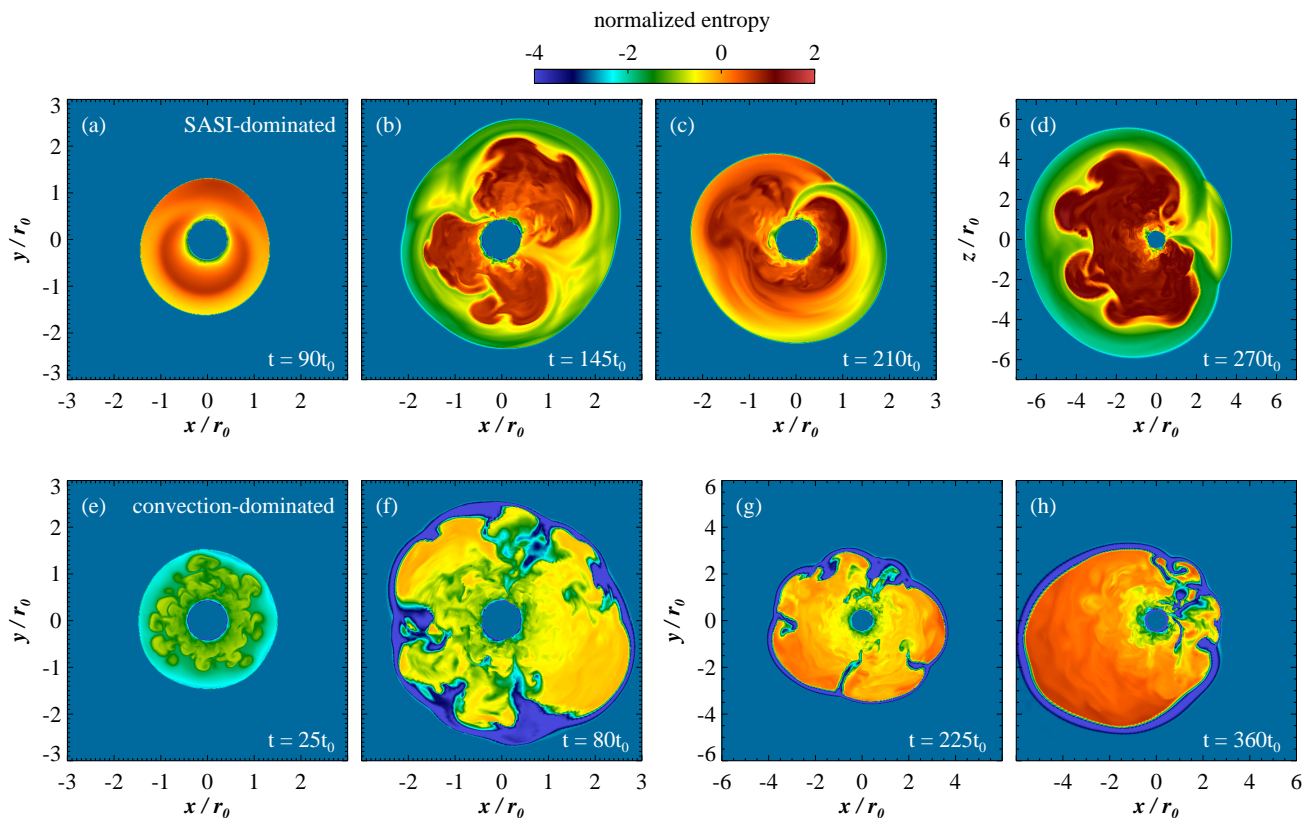


**Figure 1.** Snapshots in the evolution of the marginally exploding SASI-dominated model (S08dv, top) and convection-dominated model (C07dv, bottom), both with random initial velocity perturbations. Each panel shows a slice of the entropy (eq. [3]) on the  $xy$  plane; to ease comparison, the entropy in model C07dv is normalized to the initial postshock value of model S08dv. The SASI-dominated model initially develops a sloshing mode (panel a) which saturates (panel b). The subsequent development of a spiral mode (panel c) generates a large-scale, high-entropy bubble which leads to the final runaway (panel d). The convection-dominated model initially develops small convective plumes (panel e) which gradually grow into larger structures (panels f-g), until a single dominant bubble remains (panel h). Note the different spatial scale in panels (d), (g), and (h).

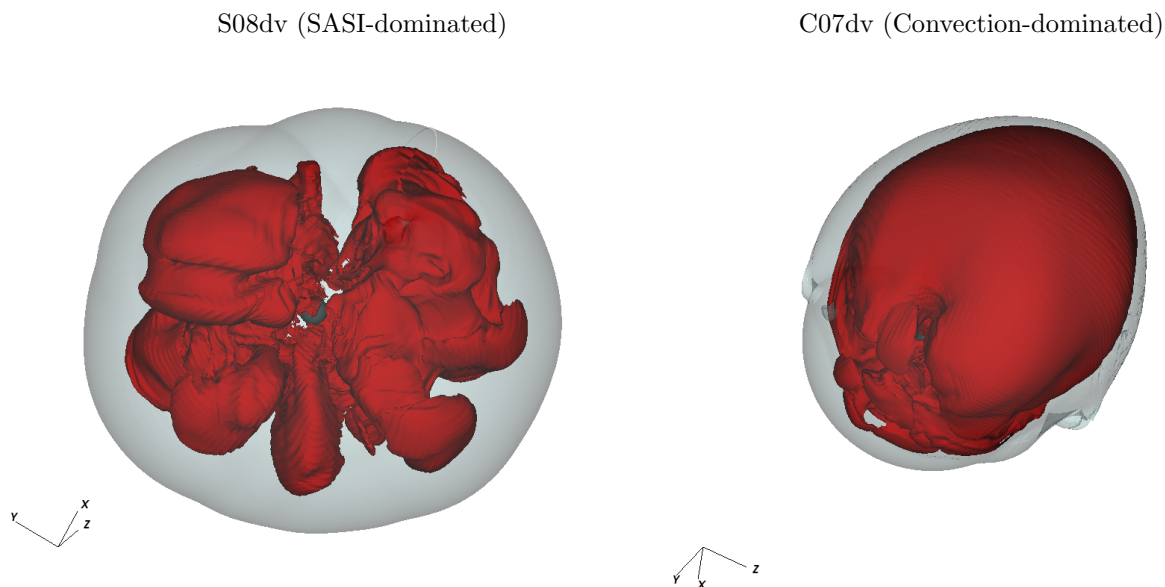


**Figure 2.** Explosion geometry near the end of the simulation for the marginally exploding SASI-dominated model (S08dv, left) and convection-dominated model (C07dv, right), corresponding to panels (d) and (h) of Figure 1. A representative entropy isosurface is shown in red, the shock is the outer light grey surface, and the neutron star is the dark grey sphere (the scale is different in the two panels).

spiral mode<sup>3</sup> survives only for a fraction of an oscillation period and the shock expansion dies down.

After this lull in shock expansion around  $t \sim 200t_0$ , a coherent spiral mode arises, growing quickly in magnitude for three full oscillations. By this time, a large high-entropy bubble has developed, and the triple-point intersects this bubble, interrupting the oscillation. Runaway does not follow immediately, however, with the bubble lingering for a period  $\sim 30t_0$ , which allows turbulence to partially break the bubble down into smaller parts. This accounts for the multiple plumes seen in Figure 1d, which become more apparent when visualizing the final explosion geometry in Figure 2. If a realistic EOS that includes the energy release from alpha particle recombination had been used, the explosion pattern would have likely frozen at a smaller radius, and the geometry would consist of a single dominant bubble.

The development of SASI activity is an optimal way to rapidly seed large-scale high-entropy bubbles. Whenever the shock expands relative to its equilibrium position, the Mach number in the frame of the shock increases, and the entropy jump correspondingly also increases (e.g., Paper I). The formation of such large-scale bubbles in 3D was also seen by Hanke et al. (2013) when the SASI was active.

The interplay between bubbles and SASI oscillations is also present in 2D (Paper I). In that case, it is found that large bubbles cut off accretion to the cooling region, which in turn breaks the SASI oscillation cycle. If bubbles are able to survive for a time longer than approximately a few SASI oscillations, a runaway expansion of the shock will ensue. In 3D, the same dynamics appears to take place, but now bubbles can have larger sizes given the lack of an axisymmetry constraint. As in 2D, failure to achieve runaway expansion in 3D appears to be related to the disruption of bubbles due to either accretion plumes and/or turbulence. We elaborate on these processes in §3.2 and §3.3.

The dynamics of convection-dominated explosions is very different. At early times, numerous small convective plumes grow out of the random initial perturbations and fill the gain region, as shown in Figure 1. The added convective stresses cause the shock to gradually expand, with convective plumes growing in size. This process continues until there is a single, dominant convective bubble that approaches the edge of the computational domain.

The increase in the shock radius due to convective stresses has been studied extensively (e.g., Murphy et al. 2013; Couch & Ott 2015). The formation of a dominant structure as the limiting case of bubble growth and/or consolidation is an intrinsic property of the non-linear Rayleigh-Taylor instability (Sharp 1984). A characteristic bubble size that subtends a solid angle  $\sim 1$  radian was predicted theoretically by Thompson (2000) as a result of a balance of buoyancy and ram pressure on the bubble, and has been further studied by Dolence et al. (2013) and Couch (2013).

The slow growth of this bubble is in part an artifact of the simplified nuclear dissociation prescription, which causes

an excess energy loss relative to the gravitational potential energy as the shock moves out (e.g., Fernández & Thompson 2009a). With a more complete EOS, runaway would have ensued at a smaller radius and hence the convective pattern would have frozen before reaching this stage (2). Nevertheless, it is interesting to note that this geometry, with a one-sided bubble, has also been observed in a simulations that include the full equation of state (Dolence et al. 2013; Lentz et al. 2015).

### 3.2 Dependence on Dimensionality and Resolution

The most interesting result of this investigation is that SASI-dominated explosions can take place at lower neutrino luminosities with increasing dimensionality. Figure 3 illustrates the magnitude of the effect, showing the evolution of the shock radius with time for systems around the critical heating rate. Models in 3D can explode at neutrino luminosities  $\sim 20\%$  lower than in 2D.

In contrast, convection-dominated systems show a much smaller difference in the critical luminosity between 2D and 3D within the spacing in  $B$  studied here ( $\sim 8\%$ ). The underlying difference will manifest itself at smaller intervals of  $B$ , but at that point the result will also depend on other factors such as the numerical resolution or the detailed form of pre-collapse perturbations (e.g., Couch & Ott 2015; Müller & Janka 2015).

Most of the work that has analyzed the dependence of 2D-3D differences in convection-dominated systems has concluded that higher resolution is detrimental for 3D (e.g., Hanke et al. 2012; Couch 2013; Takiwaki et al. 2014). This trend has been attributed to the direction in which kinetic energy flows in the turbulent cascades in 2D and 3D (Hanke et al. 2012). In our models, simply doubling the angular resolution does not prove to be very informative. The marginal 2D model at high resolution (c2d-07hr) explodes significantly earlier, as expected, but the explosion time of the marginal 3D model (C07dv-hr) is not very different<sup>4</sup>. The non-exploding 3D model with the highest heating rate (C065dv) appears to be starting an explosion on a long timescale, but due to the lack of a clear runaway we consider it a failure. Given the significant body of knowledge on this type of explosions, we will not concern ourselves further with convection-dominated systems.

The *existence* of a decrease in the critical luminosity with increasing dimensionality for SASI-dominated systems is not very sensitive to resolution, as inferred from the fact that the model with  $B = 0.009$  explodes with standard (S09dv) and high angular resolution (S09dv-hr), at times within  $\sim 10\%$  of each other, and with a heating rate that is already below the critical value in 2D. Nevertheless, the *magnitude* of this improvement appears to decrease with resolution, as found from the marginally-exploding model S08L1. When doubling the angular resolution in  $\theta$  and  $\phi$ , the model does not explode, even though very large shock excursions still occur (Figure 4). If the full EOS was employed,

<sup>3</sup> Fernández (2010) showed that spiral modes can be described as a superposition of linearly independent sloshing modes (quantified by the real spherical harmonic coefficients of the shock) which are out of phase relative to each other. This phase difference does not need to be  $\pi/2$ .

<sup>4</sup> Small variations in the explosion time are likely affected by stochastic fluctuations, and should not be taken as a primary indicator for susceptibility to explosion.

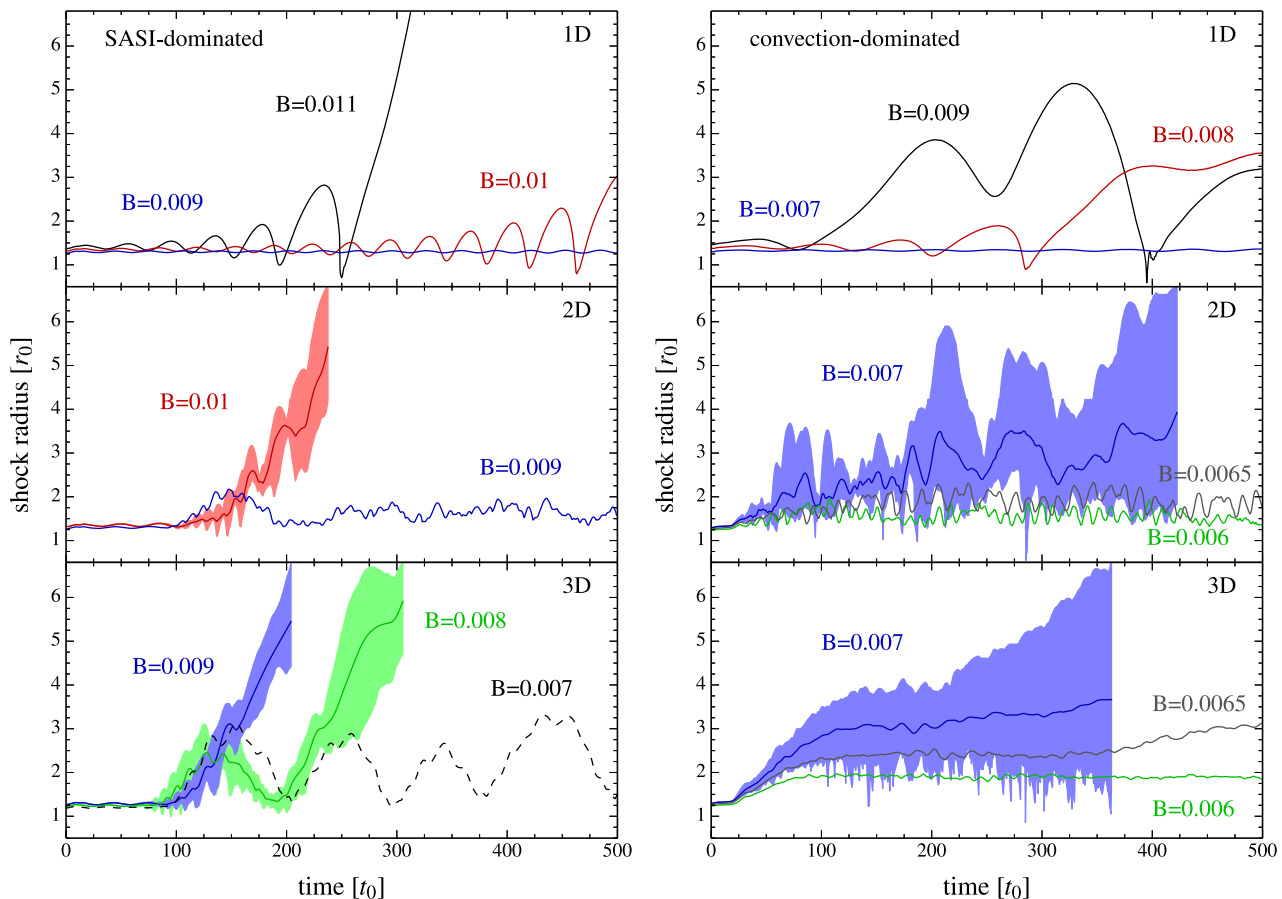


**Figure 3.** Evolution of the shock radius for SASI-dominated models (left) and convection-dominated models (right) with random initial velocity perturbations. Top, middle, and bottom panels show models around the critical transition to explosion in 1D, 2D, and 3D, respectively. For 2D and 3D models, solid lines denote the angle-averaged shock radius, and the shaded area marks the region between the minimum and maximum shock radii. Note that 3D SASI-dominated models can explode at a lower neutrino luminosity than in 2D, and that non-exploding SASI-dominated models undergo much larger shock excursions in 3D than in 2D (§3.3).

this model would likely have exploded due to the additional energy from alpha particle recombination at large radius, but within the approximations made in this study we consider it a failure. SASI-dominated systems with heating rates slightly below the critical value display much larger shock excursions in 3D than in 2D, a result that could potentially lead to further improvement in explosion conditions once the full EOS is included (c.f. §3.3). Finally, the decrease in the critical luminosity is independent on the boundary condition employed at the polar axis: model S08dv-ref, which employs a reflecting boundary condition, explodes at a time similar to the fiducial model S08dv.

We now explore quantitatively the effects of dimensionality and resolution in SASI-dominated models. As a baseline of comparison, we take the marginally-exploding model in 3D for which an initial  $\ell = 1$  sloshing SASI mode is excited via an overdense shell (S08L1). This deterministic initial perturbation allows a straightforward comparison with an identical model in 2D (s2d-08L1), and another in 3D with twice the resolution in both  $\theta$  and  $\phi$  (S08L1-hr).

A number of time-dependent diagnostics are employed in the analysis. Aside from the angle-averaged shock radius,

we compute the real  $\ell = 1$  spherical harmonic coefficients in three orthogonal (Cartesian) directions:

$$a_i(t) = \int d\Omega Y_i(\theta, \phi) r_s(\theta, \phi, t), \quad (8)$$

where  $r_s$  is the instantaneous shock surface, obtained as a pressure-gradient-weighted average for smoothness, and the real spherical harmonics basis functions are

$$Y_{\{x,y,z\}} = \sqrt{\frac{3}{4\pi}} \{\sin\theta \cos\phi, \sin\theta \sin\phi, \cos\theta\}. \quad (9)$$

The resulting coefficients can be combined linearly in order to measure sloshing modes along arbitrary axes<sup>5</sup>. Sloshing

<sup>5</sup> In the 3D models studied here, a sloshing mode is initially excited along  $\theta = \phi = 45^\circ$ . Re-defining this direction as the new  $z$  axis, the real spherical harmonic coefficients transform according to:

$$\begin{aligned} a_z &\rightarrow 0.5(a_x + a_y) + a_z/\sqrt{2}, \\ a_x &\rightarrow 0.5(a_x + a_y) - a_z/\sqrt{2}, \\ a_y &\rightarrow (a_y - a_x)/\sqrt{2}. \end{aligned}$$

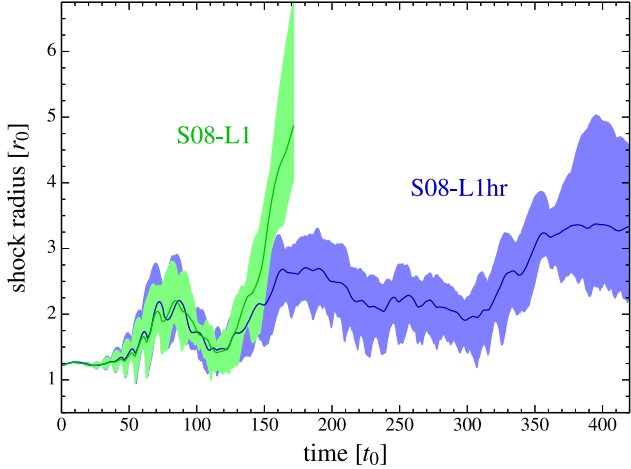


**Figure 4.** Evolution of the shock radius for two SASI-dominated models that differ only in their angular resolution. Solid lines show the angle-averaged shock radius, with the shaded area marking the space between minimum and maximum shock radius. In both cases, an  $\ell = 1$  sloshing SASI mode is initially excited at an angle to the coordinate axes ( $\theta = \phi = 45^\circ$ ). Model S08L1 is just above the critical heating rate for explosion. Doubling the resolution in both  $\theta$  and  $\phi$  (model S08L1-hr) leads to a failure within the simulated time.

SASI modes manifest as sinusoidal oscillations in these coefficients. Multiple coefficients oscillating in phase indicate sloshing modes along directions not aligned with the coordinate axes. Out-of-phase oscillations between different coefficients are the signature of spiral SASI modes (Fernández 2010). The phase difference does not have to be  $\pi/2$  for the composite mode to display the characteristic properties of a spiral mode (i.e., angular momentum redistribution). We have ignored modes with  $\ell \geq 2$  given that  $\ell = 1$  is expected to be the most unstable oscillatory SASI mode at any heating rate (e.g., Fernández & Thompson 2009b; Paper I) and to keep the analysis concise.

We diagnose the presence of bubbles with enhanced entropy in the post-shock domain by computing the instantaneous fraction of the postshock volume  $V$  occupied by fluid with entropy higher than a suitably chosen value  $s_0$  (Paper I):

$$f_V = \frac{1}{V} \int_{s_0}^{s_{\max}} \frac{dV}{ds} ds. \quad (10)$$

The creation, growth, and destruction of bubbles can be characterized quantitatively by following the evolution of  $f_V$  evaluated at multiple values of  $s_0$ .

In addition, we compute the kinetic energies in the fluctuating components of the flow

$$E_{\perp} = \int_{4\pi} d\Omega \int_{r_{\text{in}}}^{r_s} r^2 dr \frac{1}{2} \rho v_{\perp}^2 \quad (11)$$

$$E_r = \int_{4\pi} d\Omega \int_{r_{\text{in}}}^{r_s} r^2 dr \frac{1}{2} \rho (v_r^2 - \langle v_r \rangle^2), \quad (12)$$

where  $v_{\perp}$  is any non-radial velocity component ( $\theta$  and  $\phi$  when defined relative to the  $z$  axis, or *poloidal* and *toroidal* otherwise), the mean radial velocity  $\langle v_r \rangle$  is computed as an

instantaneous angle-average (e.g., Hanke et al. 2013), and the inner radius for integration  $r_{\text{in}}$  is the gain radius<sup>6</sup>.

Figure 5 shows the time-dependent diagnostics for the 2D and 3D comparison models (s2d-08L1 and S08L1, respectively). The evolution of the angle-averaged shock radius is identical up to time  $t = 60t_0$ , showing the growth and saturation of the sloshing mode that is initially excited. At this time, a sloshing mode in an orthogonal direction ( $a_x$ ) has achieved a noticeable amplitude. Thereafter, the average shock radius undergoes a larger shock excursion in 3D relative to 2D. Nonetheless, this initial expansion dies down over a time equivalent to several SASI oscillations. At time  $t = 115t_0$  a new expansion begins, and the 3D model transitions to a runaway. Meanwhile, the 2D model does not show any significant increase in its average shock radius, achieving a statistical steady-state.

The spherical harmonic coefficients indicate that the  $z$  component, initially excited, achieves the same saturation amplitude in 2D and 3D. This is expected from estimates of the effect of parasitic instabilities (Gilet et al. 2010) and also manifests in the SASI-only tests in Appendix A. The final phase of spiral mode growth that precedes explosion in 3D is characterized by a comparable amplitude in all three (out-of-phase) real spherical harmonic coefficients. Interestingly, in this second expansion phase none of the orthogonal sloshing components in 3D achieves a higher saturation amplitude than the 2D mode except after runaway expansion has set in.

Also shown in Figure 5 are the non-radial kinetic energies in the gain region. Initially, the poloidal kinetic energy in 3D (defined relative to the sloshing axis excited) is identical to the  $\theta$  kinetic energy in 2D. The energies begin to evolve differently once the  $a_x$  and  $a_y$  modes are excited, manifesting as an increase in the toroidal kinetic energy. This toroidal energy decreases as the poloidal energy saturates, at the time when the shock is retracting. The sum of poloidal and toroidal energies remains comparable to the  $\theta$  energy in 2D. Once the spiral mode achieves noticeable amplitude at  $t \sim 100t_0$ , both toroidal and poloidal energies increase monotonically. The time at which the final expansion of the shock begins coincides with the time when the sum of the non-radial kinetic energies in 3D exceeds that in 2D. By the end of the exploding simulation, this difference is a factor of several.

The volume fraction diagnostic shows that in fact the 2D model achieves larger overall fractions of the volume with high entropy than the 3D model. This would normally indicate that the 2D model achieves more favorable conditions for explosion. Upon closer inspection, however, we find that while the 2D model contains structures with higher entropy than in the 3D model, these structures occupy disconnected volumes, as shown by the  $xz$  entropy slices in Figure 6a-b. These structures also live for a shorter time, as indicated by the oscillatory pattern in the  $f_V$  diagnostic for the 2D model. Thus, achieving explosion conditions is not only related to the size of the bubbles or the magnitude of the entropy in

<sup>6</sup> When comparing models with and without heating (§3.3), the inner radius for integration is taken to be that where the angle-averaged sound speed is maximal; c.f. Paper I.



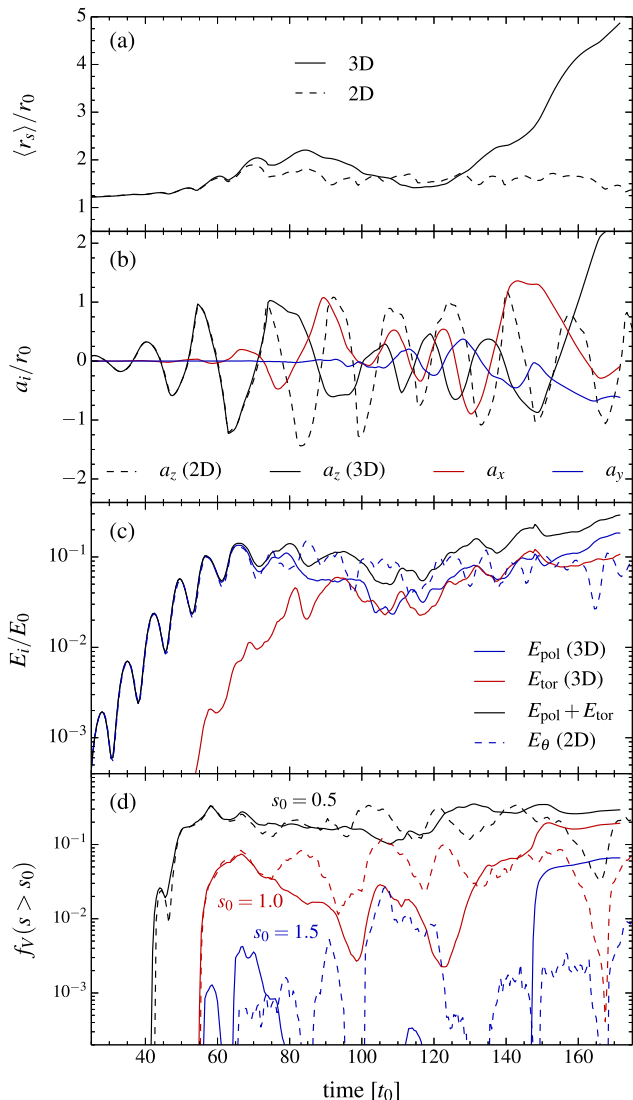


**Figure 5.** Comparison between two SASI-dominated models that differ only in their dimensionality: S08L1 (3D, marginally exploding) and s2d-08L1 (2D, non-exploding). In both cases, an  $\ell = 1$  sloshing mode is initially excited; for the 3D model, the sloshing axis is along  $\theta = \phi = 45^\circ$ . *Panel (a)*: Average shock radius. *Panel (b)*: Real spherical harmonic coefficients (eq. [8]) defined relative to the initial sloshing axis in 3D or along the symmetry axis in 2D. *Panel (c)*: Non-radial kinetic energies. In 3D, the poloidal and toroidal directions are defined relative to the initial sloshing axis. *Panel (d)*: Fraction of the post-shock volume that has entropy higher than a given value  $s_0$  (eq. [3]), as labeled. The solid and dashed lines correspond to the 3D and 2D, models, respectively.

these structures, but also involves the time during which these structures can survive.

Regarding the effect of resolution, Figure 7 shows the diagnostic quantities for the two 3D models that differ only in their angular resolution, one exploding (S08L1) and the other non-exploding (S08L1-hr; c.f. Figure 4). The evolution of both models is qualitatively very similar until  $t \simeq 130t_0$ , after which the evolution bifurcates. The spherical harmonic coefficients show that while the evolution of the sloshing mode that was initially excited is very similar in both cases,

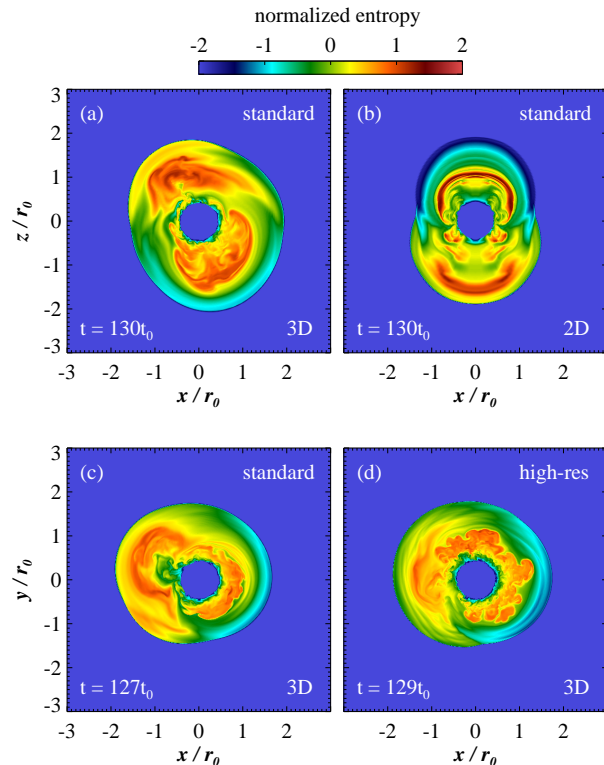


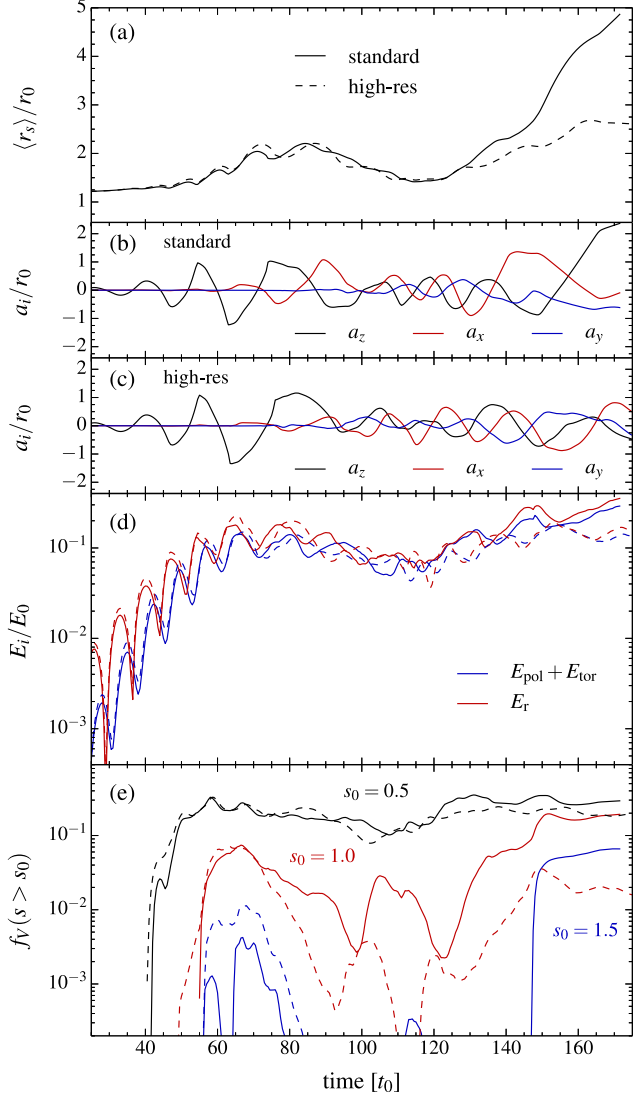
**Figure 6.** Entropy slices in SASI-dominated models with the same parameters and initial conditions except dimensionality and/or resolution, as labeled. *Panels (a-b)*: Slices on the  $xz$  plane for 3D and 2D models. In the former, the plane is defined relative to the sloshing mode that is initially excited ( $\theta = \phi = 45^\circ$ ). While the 2D model reaches higher entropy, the sizes of the bubbles are smaller than in 3D. *Panels (c-d)*: Slices on the  $xy$  plane in 3D models with different resolution. The plane is perpendicular to the sloshing axis. The model with high angular resolution displays a larger degree of small-scale turbulence. Compare with Figs. 5 and 7.

the amplitude of  $a_x$  is larger in the lower resolution model at the time when explosion begins. In other words, a stronger spiral SASI mode can be the difference between explosion and failure.

This subtle difference is also reflected in the kinetic energies in the gain region. Both radial and non-radial energies are initially larger in the higher resolution model, as expected from the known dependence of the SASI growth rates with angular resolution (Fernández & Thompson 2009b). The energies in the two models remain close to each other during the period of shock retraction, and bifurcate only around the time when runaway sets in.

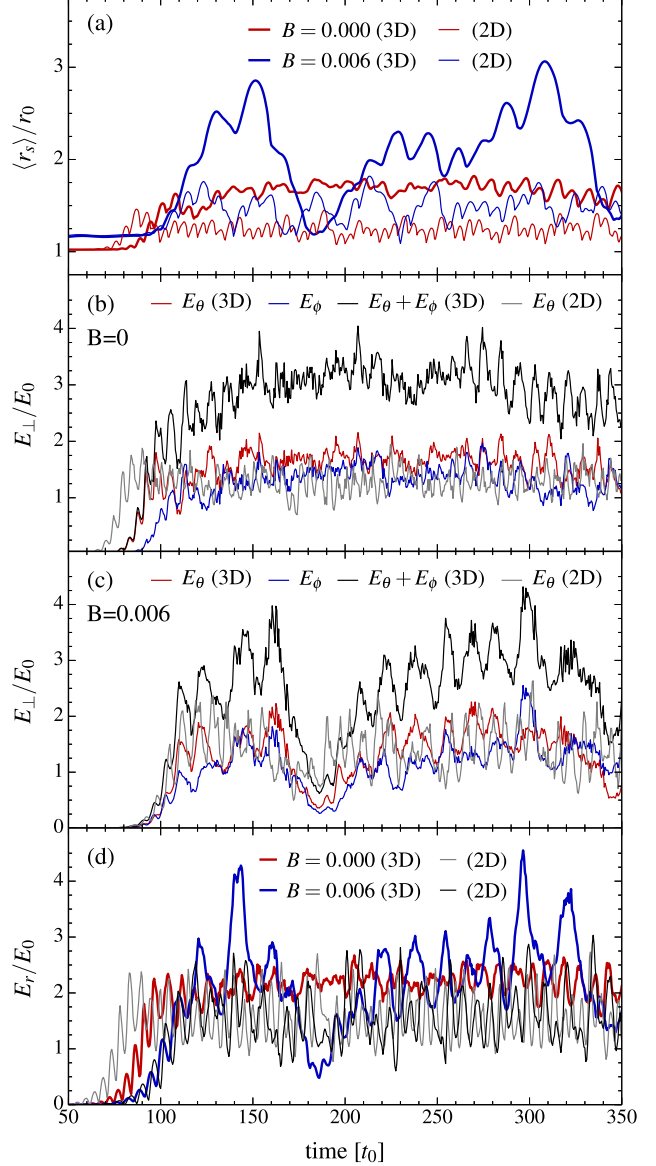
The volume fraction diagnostic  $f_V$  is more informative in this case, indicating that the lower resolution model is able to maintain a larger volume with high-entropy relative to the high-resolution model after time  $t \simeq 70t_0$ .

Figure 6 also shows two snapshots of the entropy on the  $xy$  plane (defined relative to the initially excited sloshing mode) at similar stages prior to the bifurcation in the evolution of these two models. The snapshots suggest that the smaller scale turbulence in the higher resolution model is related to more efficient fragmentation of high-entropy bub-



**Figure 7.** Comparison between two SASI-dominated models that differ only in their angular resolution: S08L1 (standard resolution, marginally exploding) and S08L1-hr (high resolution, non-exploding). In both cases, a sloshing mode along  $\theta = \phi = 45^\circ$  is initially excited. *Panel (a)*: Average shock radius. *Panels (b) and (c)*: Real spherical harmonic coefficients (eq. 8) defined relative to the initial sloshing axis. *Panel (d)*: Transverse and radial kinetic energies (eq. [11] and 12). *Panel (e)*: Fraction of the post-shock volume that has entropy higher than a given value  $s_0$  (eq. [10]), as labeled, with the entropy is defined as in equation (3). Solid and dashed lines correspond to standard and high resolution, respectively.

bles. We interpret the failure to explode in model S08L1-hr as due to the shorter life of these high-entropy bubbles given the more efficient disruption by turbulence. This interpretation is a conjecture at present, requiring further study to be established as the definitive cause for the failure of higher resolution models. An interesting question is whether this shredding of bubbles can be characterized in terms of parasitic instabilities as for SASI modes (e.g., Guilet et al. 2010).



**Figure 8.** Relation between shock expansion and kinetic energy in selected non-exploding SASI-dominated models, illustrating the effect of neutrino heating and dimensionality (models s2d-00, s2d-06, S00dv, S06dv; see Table 2). *Panel (a)*: Average shock radius. *Panel (b) and (c)*: Non-radial kinetic energy (eq. [11]) for models with  $B=0$  and  $B=0.006$ , respectively. *Panel (d)*: Radial kinetic energy in the fluctuating component of the flow (eq. [12]). The operation of spiral modes in 3D leads to a larger amount of non-radial kinetic energy than in 2D. Episodic shock excursions are related to the formation of large-scale high-entropy bubbles when neutrino heating is included. When the bubbles are shredded and an explosion fails to start, the shock retreats and the cycle resets.

### 3.3 Spiral mode with heating: large shock excursions

Another interesting result of this investigation is that SASI-dominated models in 3D that do not explode, but which are close to the critical neutrino luminosity, display shock excursions that are much larger than in their 2D counter-

parts. This effect is visible in Figure 3 for the model with  $B = 0.007$ . Here we investigate the origin of this effect, and discuss the potential for a larger difference between 2D and 3D once a realistic EOS, with alpha particle recombination, is included in the evolution.

For this analysis, we carry out two additional non-exploding models, each in 2D and 3D: one with no heating (s2d-00 and S00dv, respectively) and another with  $B = 0.006$  (s2d-06 and S06dv, respectively). Figure 8a compares the evolution of the average shock radius for these four models. Two features stand out. First, the 2D models have systematically smaller shock radii than their 3D counterparts. Second, models with heating undergo episodes in which the shock executes large excursions. In the 2D model with heating, these excursions last for a shorter time and have smaller amplitudes than in 3D.

Inspection of the 3D model with heating shows that these excursions are associated with the appearance of large-scale, high-entropy bubbles. An expansion of the shock against a supersonic incident flow leads to an increase in the Mach number in the frame of the shock, leading to a larger entropy jump and hence to the formation of a high-entropy bubble with a size comparable to the portion of the shock that is expanding (e.g., Paper I). As is the case in 2D, the formation of large enough bubble leads to the interruption of the SASI cycle. If a runaway expansion fails to ensue, the bubble is shredded, either by turbulence or by external bulk motions (e.g., downflows), and the shock retracts. A larger shock radius means a larger volume subject to neutrino heating where high-entropy bubbles can grow.

Figure 8b-c also shows the non-radial kinetic energies for the four comparison systems (c.f. eq. [11]). Given that models without heating are included in the comparison, the lower radius for computation of these energies is that where the angle-averaged sound speed is maximal (e.g., Paper I). The resulting (total) non-radial kinetic energies are larger in 3D than in 2D, whether neutrino heating is included or not. It is not surprising then that the average shock radius is larger in 3D than in 2D, as more kinetic energy inside the shock provides additional support against the ram pressure of the collapsing stellar core (e.g., Murphy et al. 2013; Couch & Ott 2015).

For models without heating, in which non-radial motions are solely driven by the SASI, the non-radial kinetic energies in the fully non-linear phase satisfy  $E_{\theta}^{3D} \sim E_{\phi} \sim E_{\theta}^{2D}$ . Hence, the spiral modes of the SASI are able to approximately double the total non-radial kinetic energy in the post-shock domain. Inspection of Figure 5b as well as tests in Appendix A indicate that the saturation amplitude of individual sloshing modes, quantified by the real spherical harmonic coefficients (eq. [9]), is very similar in 2D and 3D (this is also a prediction from the analysis of Guilet et al. 2010). Recall that two or three linearly-independent real spherical harmonic coefficients oscillating in phase are indicative of a single sloshing mode, thus their individual amplitudes will not reach the maximum possible value (their root-mean-square sum will). A spiral mode appears to be able to tap into the full amplitude of its individual constituent (orthogonal) sloshing modes, hence roughly doubling the kinetic energy.

For the cases with heating, the non-radial kinetic energy in 2D is slightly larger than the individual  $\theta$  or  $\phi$  energies

in 3D, but still smaller than their sum. The episodic shock excursions in 3D are concurrent with increases in the non-radial kinetic energy. However, the overall magnitude of the non-radial 3D energies are very close to those of the model without heating.

The key feature that sets apart the model with large shock excursions from others is the magnitude of the fluctuating radial kinetic energy (eq. [12]), as shown in Figure 8d. Whereas in 2D the radial kinetic energy is comparable to that in the  $\theta$  direction whether heating is included or not, in 3D the total non-radial kinetic energy exceeds its radial counterpart by about  $\sim 50\%$  during most of the time. However, during episodes of transient shock expansion, the radial kinetic energy of the model with  $B = 0.006$  shows large increases that match or even exceed the total non-radial kinetic energy.

We interpret this increase in radial kinetic energy as being a consequence of the large high-entropy bubbles having internal structure and being convective, as can be seen from Figure 1. In a fluid where buoyant convection operates, the relation  $E_r \simeq E_{\theta} + E_{\phi}$  holds (Murphy et al. 2013). The fact that the radial kinetic energy remains large only for a short period of time is related to the short lifetime of the large-scale bubbles, which are shredded prior to shock retraction.

The large shock excursions shown by the 3D SASI-dominated models with neutrino luminosities close to critical hold promise for further reductions in this critical heating rate once a more realistic EOS is included. If the effect of alpha particle recombination is included, the ratio of nuclear dissociation energy to gravitational potential energy at the shock does not increase with radius (e.g. Fernández & Thompson 2009a), and hence the system loses less energy upon expansion. A characteristic radius  $r_{\alpha}$  where this effect becomes dynamically important is that were the nuclear binding energy of alpha particles equals the gravitational binding energy,

$$r_{\alpha} \simeq 254M_{1.3} \text{ km.} \quad (13)$$

Taking  $r_0 = 100$  km for a characteristic stalled shock radius without neutrino heating, shock excursions such as those of model S06dv should very likely lead to a runaway expansion. This conjecture will be tested in future work.

## 4 SUMMARY AND DISCUSSION

We have investigated the properties of SASI- and convection-dominated core-collapse supernova explosions in three dimensions using parameterized hydrodynamic simulations. This approach allows to isolate the effect of hydrodynamics instabilities on the explosion mechanism from uncertainties in progenitor models, the EOS of dense matter, or an incomplete treatment of neutrino effects. By generating sequences of models well within the parameter regimes where either the SASI or convection dominates, we characterized the effect of adding a 3rd spatial dimension on the dynamics. Our main results are the following:

1. – SASI-dominated explosions do exist in 3D, and their evolution is qualitatively different from convection-dominated explosions. (Fig. 1). For systems in which both

the mass accretion rate and protoneutron star radius change slowly relative to the thermal time in the gain region, the value of the convection parameter  $\chi$  (eq. [7]) at the time when the shock stalls is a good predictor of the explosion path to be taken by the system, if the neutrino luminosity is high enough.

2. – SASI-dominated systems can explode with a lower neutrino luminosity in 3D than in 2D (Fig. [3], Table 2). This difference is related to the ability of spiral modes to generate more non-radial kinetic energy than a single sloshing mode, resulting in a larger average shock radius and hence generating more favorable conditions for the formation of large-scale, high-entropy bubbles (Fig. 5). For the baseline angular resolution employed here ( $\Delta\theta \simeq \Delta\phi \simeq 2^\circ$  at the equator), the critical neutrino luminosity in 3D is  $\sim 20\%$  lower than in 2D.

3. – Convection-dominated explosions show a much smaller change in the critical heating rate with increasing dimensionality. In fact, no significant difference was found between 2D and 3D for the spacing in heating rate explored here ( $\sim 8\%$ ). This result is consistent with previous studies (e.g., Hanke et al. 2012). Doubling the angular resolution of the marginally exploding models yields earlier explosions in 2D and minor changes in explosion time for 3D (Table 2).

4. – Doubling the angular resolution in  $\theta$  and  $\phi$  decreases the difference in critical neutrino luminosity between 2D and 3D for SASI-dominated explosions (Figs. 4 and 7). We interpret this reduction as a consequence of the higher efficiency of 3D turbulence at higher resolution for disrupting the large-scale, high-entropy bubbles needed to launch an explosion (Fig. 6). The exact dependence of this increase in the critical neutrino luminosity with resolution in 3D was not obtained, but based on the healthy explosion obtained in a 3D model with 10% lower heating rate than the marginal 2D model ( $B = 0.009$ , both at high resolution; Table 2), we infer that this difference is shallower than  $B_{\text{crit}}^{3D} \propto (\Delta\theta\Delta\phi)^{-0.085}$ . This sensitivity to resolution also highlights the need for a better understanding of the systematic uncertainties associated with the use of finite volume methods to model supernova flows, in which the spatial resolution is limited by current computational resources (e.g., Porter & Woodward 1994; Radice et al. 2015).

5. – Non-exploding SASI-dominated models have larger average shock radii in 3D than in 2D, which we interpret to be a consequence of the higher non-radial kinetic energy generated by spiral modes (Fig. 8). While the saturation of individual sloshing modes appears to be very similar in 2D and 3D (Fig. 5, Appendix A), a spiral mode can generate more kinetic energy than a single sloshing mode (e.g., Figure A2). This result is in agreement with the findings of Hanke et al. (2013), and in conflict with the interpretation of Iwakami et al. (2008) that saturation in 3D is smaller because the same amount of kinetic energy is shared between a larger number of modes. The exact limiting factor to the energy available for a spiral mode was not investigated here, but it is worth pursuing in future studies.

6. – Very large shock excursions can result in 3D when the heating rate is close to (but lower than) the critical value for an explosion in SASI-dominated models. These excursions are simultaneous with the appearance of high-entropy bubbles generated by the expanding shock, and are smaller in magnitude (by a factor  $\sim 2$ ) in 2D. The non-radial kinetic energy is generally larger than the radial kinetic energy when spiral modes operate, except when large bubbles are formed and the shock expands, in which case the relation  $E_r \sim E_\theta + E_\phi$  holds. We conjecture that this is due to the internal structure of bubbles, which is likely convective. The large shock excursions open the possibility of further improvements in explosion conditions in 3D when the effect of alpha particle recombination is included.

While the behavior of the  $27M_\odot$  model of Hanke et al. (2013) during the time when spiral modes operate appears to be consistent with our results, the period of spiral-SASI-driven shock expansion is too short to make an unambiguous parallel. The maximum amplitudes of the sloshing modes involved and the total transverse kinetic energies exceeded the values obtained in 2D for a brief period. Unfortunately, just as the shock begins to turn around and grow at a rate faster than in 2D, the Si/SiO composition interface is accreted through the shock, triggering a large expansion that makes the model convective again.

The relation between growth of the non-radial kinetic energy and approach to explosion was noted by Murphy & Meakin (2011) and Hanke et al. (2012). Intuitively, one expects accreted material to spend more time in the gain region when the flow is non-radial and the gain region is larger due to the larger shock radius (e.g., Murphy & Burrows 2008). An interesting way to think about the reduction in critical neutrino luminosity when going from 1D to 2D/3D is that due to the non-laminar stresses, a given shock radius requires less thermal pressure to be maintained and thus less neutrino heating to drive an expansion from this position than if the flow were laminar (Couch & Ott 2015). This is equivalent to saying that, in analogy with accretion disks, the effective gravity felt by the fluid inside the shock is smaller due to the action of bulk or turbulent stresses,

$$g_{\text{eff}} \sim \frac{GM(r)}{r^2} - \frac{v_{\text{fluct}}^2}{r}, \quad (14)$$

where  $v_{\text{fluct}}^2 = \langle v_r^2 - \langle v_r \rangle^2 + v_\theta^2 + v_\phi^2 \rangle$ . This is also consistent with the critical r.m.s. Mach number threshold proposed by Müller & Janka (2015). Regardless of the conceptual framework used to interpret it, the improved ability of spiral modes to extract non-radial kinetic energy from the accretion flow appears to improve conditions for explosion.

While we have found a region of parameter space in which 3D is more favorable to explosion than 2D, it is fair to ask whether this parameter space is actually realized in Nature. The  $27M_\odot$  model of Hanke et al. (2013) is genuinely SASI-dominated until the Si/SiO interface is accreted, as diagnosed by the evolution of  $\chi$ , which lingers around 2 before the composition interface falls through the shock. In contrast, the same progenitor evolved by Couch & O’Connor (2014) (using  $f_{\text{heat}} = 1.00$ ) yields  $\chi$  closer to 3 when the shock stalls, showing that the treatment of neutrino transport can be influential in determining the evolution-

ary path taken by the system. More generally, our knowledge of two key external ingredients to the supernova mechanism is by no means complete. First, progenitor stars are likely to be members of interacting binary systems (e.g., Sana et al. 2012; Smith 2014), intrinsically multidimensional (e.g., Arnett & Meakin 2011; Couch et al. 2015) and with a degree of rotation yet to be convincingly established (e.g., Fuller et al. 2015). Second, the EOS of matter at supranuclear densities remains uncertain despite significant recent progress (e.g., Lattimer 2012).

In the end it may well turn out to be that, as suggested by Abdikamalov et al. (2014), the SASI is relevant mostly for high accretion rate progenitors that fail to explode. Because neutron star formation generally precedes collapse to a black hole (e.g., O’Connor & Ott 2011), the same predictions for the neutrino and gravitational wave emission for systems with strong SASI activity (e.g., Müller et al. 2013; Tamborra et al. 2014) should apply. In fact, the higher accretion rates in failed systems are expected to yield a more intense neutrino signal than exploding models (O’Connor & Ott 2013). This should improve prospects for identification of a Galactic event even if dedicated surveys (e.g., Kochanek et al. 2008) fail to detect the electromagnetic signature predicted for these systems (Nadezhin 1980; Lovegrove & Woosley 2013; Piro 2013; Kashiyama & Quataert 2015).

If on the other hand progenitor properties turn out to favor SASI-dominated explosions once uncertainties have been resolved, the effect of pre-collapse perturbations on the development of a spiral SASI mode remains as a potential obstacle. The advective-acoustic cycle involves the interplay of coherent perturbations that require a relatively smooth background flow to develop. The work of Guilet et al. (2010) indicates that large amplitude perturbations can disrupt the acoustic feedback in the cycle and lead to ineffective growth. Furthermore, the work of Müller & Janka (2015) suggests that if physically-motivated pre-collapse perturbations are used, the shock acquires a nearly static asphericity, with detrimental conditions for the development of the SASI (but providing an alternative channel for the generation of non-radial kinetic energy).

Our results prove the principle that SASI-dominated explosions can provide better conditions for explosion in 3D than in 2D. For the effect to be considered robust, however, a key set of physical ingredients needs to be added. Future work will address the response of these types of explosion to the inclusion of a realistic EOS (including nuclear recombination), rotation in the accretion flow, the feedback from the accretion luminosity on the gain region, and the time-dependence of the accretion rate and neutron star radius. These studies will help clarify issues such as the behavior of the  $20M_{\odot}$  model with sophisticated neutrino transport reported in Tamborra et al. (2014), which in 3D undergoes an extended phase of SASI activity but fails to explode, while succeeding in 2D (T. Janka, private communication).

A more realistic (but still parametric) study would also allow exploration of issues such as the elementary processes that mediate the transition to explosion (e.g., Pejcha & Thompson 2012; Fernández 2012; Müller & Janka 2015), the amount of angular momentum imparted to the neutron star by spiral modes, which depends on the mass cut at the time of explosion (e.g., Guilet & Fernández 2014)

as well as the potential for spiral modes to amplify magnetic fields (e.g., Endeve et al. 2012) in an explosion context. The results of such studies would inform the analysis of more sophisticated models, in which the high computational cost precludes a systematic exploration of parameter space.

Ultimately, the magnitude of the improvement in efficiency on the neutrino mechanism introduced by the SASI in 3D, if all conditions are favorable, is of the order of  $\sim 10\%$ . While this contribution is relatively modest, it can help to tilt systems that would be otherwise marginal towards a robust explosion (as is the case when, e.g., the neutrino cross sections are modified at the  $\sim 10\%$  level in the right direction; Melson et al. 2015a).

## ACKNOWLEDGMENTS

I thank Dan Kasen, Eliot Quataert, Thomas Janka, Thierry Foglizzo, Jérôme Guilet, Ralph Hix, Sean Couch, and John Blondin for helpful discussions and/or comments on the manuscript. The anonymous referee provided constructive comments that improved the presentation of the paper. RF acknowledges support from the University of California Office of the President, and from NSF grant AST-1206097. The software used in this work was in part developed by the DOE-supported ASC / Alliance Center for Astrophysical Thermonuclear Flashes at the University of Chicago. This research used resources of the National Energy Research Scientific Computing Center (NERSC), which is supported by the Office of Science of the U.S. Department of Energy under Contract No. DE-AC02-05CH11231. Computations were carried out at *Carver* and *Hopper* (repo m2058).

## APPENDIX A: EXTENSION OF THE SPLIT PPM SOLVER IN FLASH3.2 TO 3D SPHERICAL COORDINATES

Here we describe the extension to 3D spherical polar coordinates of the split PPM solver present in the public version of FLASH3.2. We then describe tests of this modified code. The test cases can be used to diagnose any hydrodynamics code in 3D spherical coordinates.

### A1 Implementation

The split PPM solver embedded in FLASH3.2 is based on PROMETHEUS (Fryxell et al. 1989), which implements the method of Colella & Woodward (1984). The public FLASH version requires only a few modifications to run on a grid defined in 3D spherical coordinates. The modifications are:

- (i) Allowing 3D spherical geometry in the subroutine `Hydro_detectShock`, and computing the appropriate velocity divergence;
- (ii) Modifying the ratio of time step to cell spacing  $dt/dx$  in the subroutine `hydro_1d` to account for the proper cell spacing in the azimuthal direction,  $dx_{\phi} = r \sin \theta d\phi$
- (iii) Implementing a safeguard in the subroutine `avisco`, whenever division by  $\sin \theta$  leads to singular behavior in the velocity divergence. This is the only subroutine where this divisor is evaluated at the cell face, where it can vanish if

the grid extends to the polar axis. In practice, a small floor value of  $\sin \theta$  ( $\sim 10^{-6}$ ) can be imposed.

(iv) Modifying the arguments to the subroutine `Hydro_detectShock`, called by `hy_ppm_sweep` in order to use the correct coordinates.

In addition to these basic modifications, we have experimented with two additional changes that can improve the accuracy of the code:

(i) The fictitious accelerations that account for the centrifugal and Coriolis forces in curvilinear coordinates are computed with velocities evaluated at the beginning of the time-step. For consistency with PPM, these accelerations should be time-centered. We implement this modification by evaluating 1/2 of the acceleration forward in time after the PPM update. This is straightforward because the force along a given direction depends linearly on the corresponding velocity component. Tests indicate that this modification leads to minor differences in the results.

(ii) The default reflecting boundary condition in the  $\theta$  direction at the axis can be improved by making use of the data across the axis to fill the ghost cells. For example, for the first active cell next to the axis (with center coordinate  $\theta = \theta_1$ ), the contents of its neighboring ghost cell can be set to satisfy

$$A(r, -\theta_1, \phi) = A(r, \theta_1, \phi + \pi), \quad (\text{A1})$$

where  $A$  is an arbitrary variable. The sign of the transverse velocities  $v_\theta$  and  $v_\phi$  must be changed to account for the sign change in the corresponding unit vectors across the axis. This type of operation requires ghost cell exchange between processors that contain cells located at opposite sides of the axis.

Additional changes are needed only when using a non-uniform grid. These changes involve generating the non-uniform coordinates, using the exact cell volumes and areas (instead of linearized approximations), and passing the correct vector of cell spacings to the PPM routines instead of a constant value. These modifications are further described in Fernández (2012).

## A2 Tests

We test the reliability of the hydrodynamic solver in 3D by using the parameterized accretion shock setup described in §2.2 without neutrino heating. The system is then only unstable to the SASI, with no convection. By exciting individual modes of system, the numerical solution can be compared directly with predictions from linear stability analysis (Fernández & Thompson 2009b).

The parameters of the setup are an initial ratio of star to shock radius  $r_*/r_0 = 0.5$ , adiabatic index  $\gamma = 4/3$ , no nuclear dissociation at the shock ( $\varepsilon = 0$ ), and the same parameterized neutrino source term in equation (1) but without neutrino heating ( $B = 0$ ). This is the same set of parameters used in Fernández (2010), which has the advantage that only the fundamental  $\ell = 1$  SASI mode is unstable. In the absence of rotation, the modes are degenerate in  $m$ , serving as a good diagnostic of the isotropy of the code. This is a global problem involving subsonic flow, where a delicate balance between pressure gradients and gravity needs

**Table A1.** Test models evolved. Columns from left to right show model name, type of initial perturbation applied, use of a hybrid Riemann solver at shocks, type of boundary condition used at the polar axis in the  $\theta$  direction, and root-mean-square amplitude of the  $\ell = 1$  spherical harmonic coefficient along the excited dipole axis (for reference, the 2D value is  $\Delta a_1/r_0 = 0.544$ ). The initial perturbation has the form of an overdense shell with angular dependence given by a real spherical harmonic:  $Y_z, Y_x$ , or  $Y_d \equiv Y_z/\sqrt{2} + (Y_x + Y_y)/2$ . When no explicit perturbation is applied, initial transients result in a spherically-symmetric perturbation. For comparison, 1D and 2D versions of each model are also evolved.

Model	Pert.	Hybrid?	Axis Bnd.	$\Delta a_1/r_0$
T-L0-hyb	none	yes	reflect	...
T-L0-std		no		...
T-L1z-ref	$Y_z$	yes	reflect	0.534
T-L1x-ref	$Y_x$			0.530
T-L1d-ref	$Y_d$			0.544
T-L1z-trm	$Y_z$	yes	transmit	0.533
T-L1x-trm	$Y_x$			0.526
T-L1d-trm	$Y_d$			0.552

to be maintained. Any obvious errors in the code manifest immediately.

The tests differ in the type of initial perturbations applied and in the boundary condition at the axis. SASI modes are excited by dropping an overdense shell with a given angular dependence, as described in §2.2. For comparison, 1D and 2D versions are also evolved. We used the standard angular resolution ( $\Delta\theta \simeq \Delta\phi \simeq 2^\circ$  at the equator, §2.2) for all tests. Table A1 summarizes the parameters of each test simulation. Model names start with T for “test”, and then indicate the type of initial perturbation and boundary condition employed (e.g., T-L1z-ref corresponds to  $\ell = 1$  sloshing mode along the  $z$  axis, with reflecting boundary condition at the axis).

The tests probe four aspects of the code: (1) the ability to maintain spherical symmetry and agreement with 1D and 2D versions, (2) the ability to maintain axisymmetry and its agreement with the 2D version, (3) the effect of using a reflecting or ‘transmitting’ boundary condition at the axis, and (4) the isotropy of the code in 3D (symmetry along an arbitrary axis).

### A2.1 Spherical symmetry

The first test simply lets the accretion flow evolve in the absence of perturbations. Initial transients generate an  $\ell = 0$  perturbation that damps on a timescale of several  $100t_0$ , because the corresponding SASI mode is stable.

To achieve a clean test setup, it is important to damp numerical perturbations that arise spontaneously. We find that significant numerical noise arises from the shock in 3D models if the standard PPM solver is used in all cells. This is illustrated in Figure A1, which shows the angle-averaged shock radius for models T-L0-std and T-L0-hyb, as well as the magnitude of the non-radial kinetic energies in the  $\theta$  and  $\phi$  directions.

It is well known that a hybrid Riemann solver can eliminate numerical problems at shocks aligned with the grid,

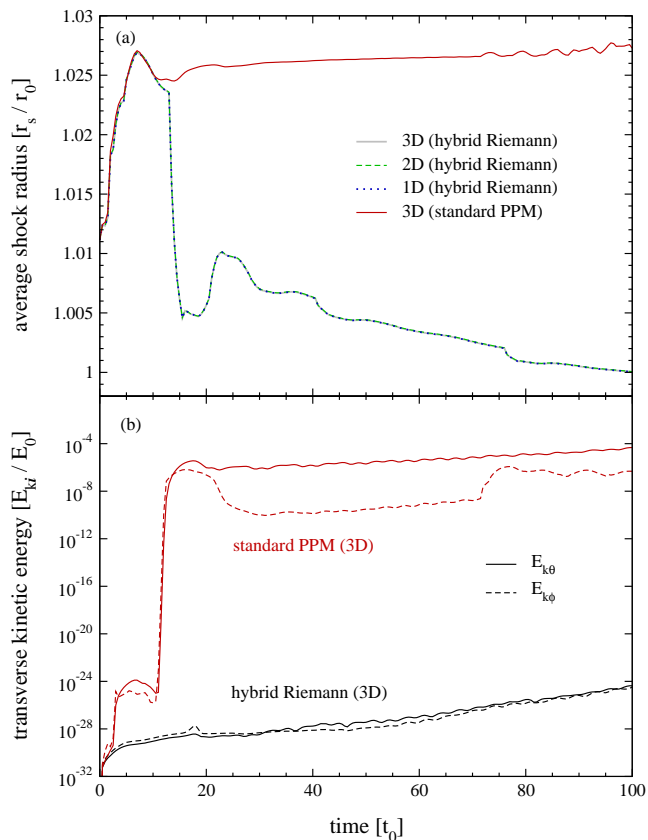


**Figure A1.** Test of the ability of the code to maintain spherical symmetry in the absence of explicit perturbations. *Panel (a)*: Average shock radius as a function of time for 1D, 2D, and 3D models without initial perturbations. Also shown is a 3D model that does not use the hybrid Riemann solver. *Panel (b)*: Transverse kinetic energies for 3D models without perturbations, showing hybrid Riemann (black) and standard split PPM (red). Using the hybrid Riemann solver keeps spurious non-radial velocity perturbations from growing too much above the numerical noise.

particularly the odd-even decoupling instability and carbuncle phenomenon (Quirk 1994). FLASH3.2 allows the use of a HLLC solver inside shocks to increase dissipation and damp these numerical instabilities. Figure A1 shows that when this hybrid Riemann solver is used, spurious numerical perturbations (quantified by the non-radial kinetic energies) remain close to the numerical noise, growing slowly.

Using the hybrid Riemann solver also enables excellent agreement between 1D, 2D, and 3D. This agreement is reached only above a certain radial resolution, however, due to the steep density gradient at the base of the flow, which results in the irregular misidentification of shocks at low resolution. The baseline radial resolution adopted in the study (a fractional radial spacing  $\Delta r/r \simeq 0.45\%$  or  $0.26^\circ$ ) is the lowest resolution for which this agreement between different dimensions is reached.

### A2.2 Symmetry around the $z$ axis

The next test probes the ability of the code to maintain axisymmetry around the  $z$  axis. We evolve a 3D model for which an  $\ell = 1$  sloshing mode is excited along the  $z$  axis

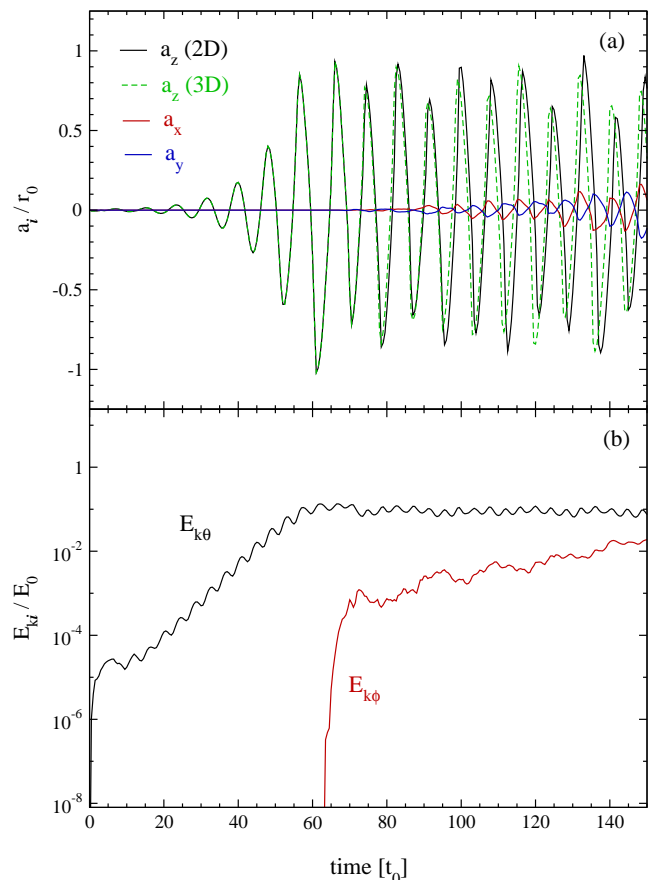


**Figure A2.** Test of the ability of the code to maintain axisymmetry. *Panel (a)*: Real spherical harmonic coefficients (eq. [8]) for model T-L1z-ref and an identical run in 2D. In both cases an  $\ell = 1$  SASI sloshing mode along the  $z$  axis is initially excited. The code remains axisymmetric until the SASI saturates. *Panel (b)*: Kinetic energies in the polar ( $\theta$ ) and azimuthal ( $\phi$ ) directions for model T-L1z-ref. Upon saturation of the SASI, the azimuthal kinetic energy grows rapidly from numerical noise and triggers the growth of modes orthogonal to the  $z$  axis.

(T-L1z-ref). Given our choice of parameters, only the fundamental  $\ell = 1$  mode should be unstable and therefore a clean sinusoidal oscillation of the corresponding  $\ell = 1$  spherical harmonic coefficient (eq. [8]) should be obtained.

Figure A2a shows the evolution of the  $z$  real spherical harmonic coefficient (eq. [8]) for model T-L1z-ref, and compares it with a 2D version that excites an  $\ell = 1$  mode in the same way. The 3D model remains axisymmetric up to the moment when the sloshing SASI mode saturates at  $t \simeq 60t_0$ . Thereafter, the azimuthal kinetic energy experiences rapid growth out of numerical noise, as shown in Figure A2b, leading to the excitation of transverse sloshing modes in the  $x$  and  $y$  directions. This growth in transverse motion originates in numerical noise at the polar axis. Nonetheless, the sloshing mode along the  $z$  direction remains nearly identical between 2D and 3D up to a time  $t \simeq 70t_0$ , or  $\sim 24,000$  time steps. At later times the primary difference lies in the phase of the oscillation.

The rms fluctuation in the  $a_z$  coefficient between  $t = 75$  and  $150t_0$  is  $\Delta a_1 / r_0 = 0.544$  and  $0.534$  in 2D and 3D, respectively, with a relative difference of 2% in favor of 2D. Also,

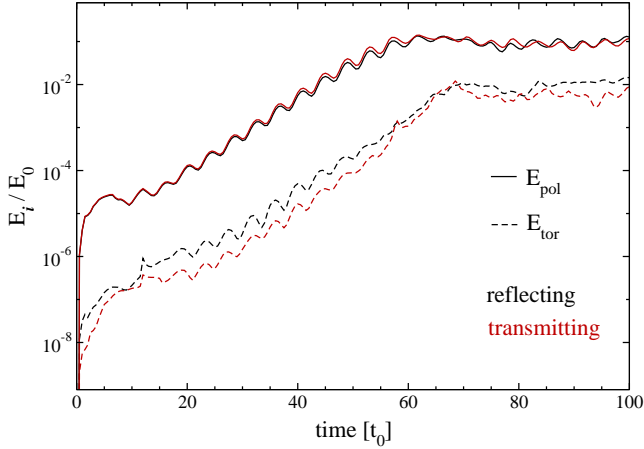


**Figure A3.** Non-radial kinetic energies – defined relative to the  $x$ -axis (eq. A2 and A3) – as a function of time for models T-L1x-ref (black lines) and T-L1x-trm (red lines), in which a sloshing SASI mode along the  $x$ -axis is initially excited, and which use reflecting and transmitting boundary conditions in the  $\theta$  direction at the axis, respectively. Solid lines show poloidal and dotted lines toroidal kinetic energy.

note that the difference in phase between the real spherical harmonic coefficients of the 3D model shows that a spiral mode is triggered.

### A2.3 Axis boundary condition

To obtain a quantitative measure of the improvement gained by using a ‘transmitting’ boundary condition in  $\theta$  (eq. A1) instead of a reflecting  $z$  axis, we evolve two models in which an  $\ell = 1$  sloshing mode along the  $x$  axis is excited.

As a diagnostic, we define poloidal and toroidal velocities relative to the  $x$ -axis:

$$v_{\text{pol}} = \frac{xy}{r\varrho}v_y + \frac{xz}{r\varrho}v_z - \frac{\varrho}{r}v_x \quad (\text{A2})$$

$$v_{\text{tor}} = -\frac{z}{\varrho}v_y + \frac{y}{\varrho}v_z, \quad (\text{A3})$$

with  $\varrho = \sqrt{y^2 + z^2}$ . These velocities are the analog of  $v_\theta$  and  $v_\phi$ , respectively. In theory, the sloshing mode should remain symmetric around the  $x$  axis, with the toroidal velocity  $v_{\text{tor}}$  serving as a diagnostic for numerical errors.

Figure A3 shows the evolution of the poloidal and toroidal kinetic energies in models T-L1x-ref and T-L1x-trm, constructed with the corresponding velocities defined in equation (A2) and (A3). In contrast to the sloshing mode along the  $z$  axis (Fig. A2), for which the azimuthal kinetic energy undergoes rapid growth only after the primary SASI mode has saturated, the toroidal kinetic energy in both models with an  $x$  sloshing SASI mode grows exponentially from the beginning. This illustrates the larger amount of numerical noise experience by this mode given the grid geometry.

Using the transmitting boundary condition results in a lower amplitude of the toroidal kinetic energy at early times, by a factor of several, relative to using a reflecting boundary condition. Nonetheless, both types of boundary condition lead to very similar results in the evolution of the primary mode. The lower level of noise motivates the use

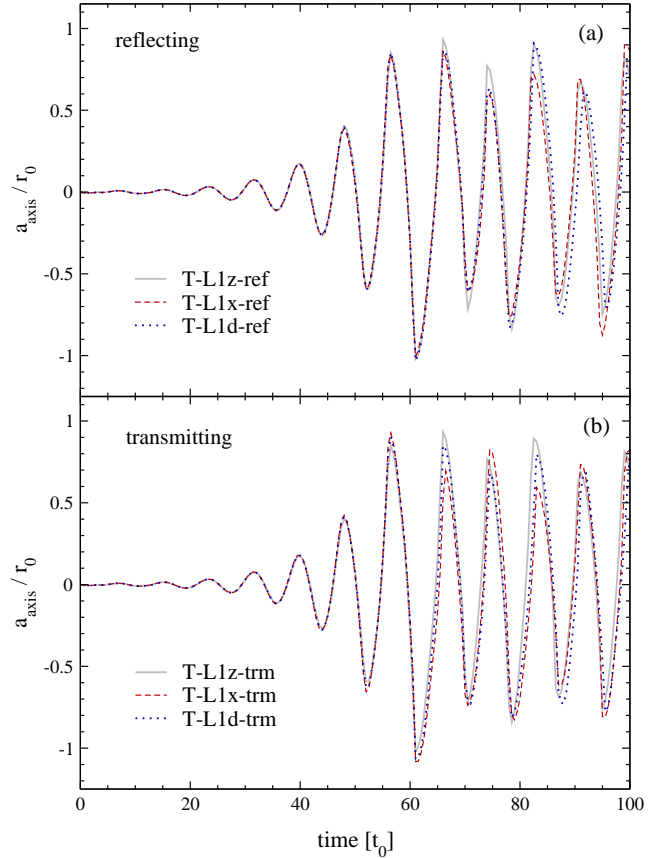


**Figure A4.** Test of the isotropy of the code. Curves show the real spherical harmonic coefficient (eq. [8]) corresponding to the axis along which a sloshing SASI mode is initially excited:  $\hat{z}$  (solid gray),  $\hat{x}$  (dashed red), and a diagonal axis ( $\hat{z}/\sqrt{2} + [\hat{x} + \hat{y}]/2$ , dotted blue). The top panel shows models that use a reflecting boundary condition in the  $\theta$  direction at the polar axis, and the bottom panel shows models that employ a transmitting boundary condition (§A2.3).

of the transmitting boundary condition as the default for production runs.

### A2.4 Symmetry along an arbitrary axis: isotropy

The final test diagnoses the isotropy of the code, which we assess by comparing the evolution of sloshing SASI modes excited along different directions: (1) the  $z$  axis, which is the natural symmetry axis of the grid given the coordinate system, (2) the  $x$  axis, which while orthogonal to the  $z$  axis is still aligned with a coordinate line on the equatorial plane, and (3) a diagonal axis defined by

$$\hat{d} = \frac{1}{\sqrt{2}}\hat{z} + \frac{1}{2}(\hat{x} + \hat{y}). \quad (\text{A4})$$

This direction lies along  $\theta = \phi = 45^\circ$ , and hence it is not aligned with any cartesian coordinate direction.

Figure A4 shows the real  $\ell = 1$  spherical harmonic coefficients (eq. [8]) along the corresponding sloshing axis for the last six models of Table A1. The evolution is identical in all cases up to the point where the primary SASI mode saturates, demonstrating the correctness of the implementation.



Models that use a reflecting boundary condition at the axis show mutual agreement in the non-linear phase for a longer time relative to models with a ‘transmitting’ axis. This agreement extends particularly to the maximum amplitude of the sloshing mode. In contrast, models with ‘transmitting’ boundary condition show closer agreement in the oscillation phase at late times, but the amplitudes are not identical. The root-mean-square fluctuation of the real spherical harmonic coefficient, computed between  $t = 75$  and  $150t_0$  is shown in Table A1. All values are within a few percent of each other, and within a few percent of the 2D value (0.544).

## REFERENCES

- Abdikamalov, E., et al. 2014, ApJ, in press, arXiv:1409.7078
- Arnett, W. D., & Meakin, C. 2011, ApJ, 733, 78
- Bethe, H. A. 1990, Reviews of Modern Physics, 62, 801
- Bethe, H. A., & Wilson, J. R. 1985, ApJ, 295, 14
- Blondin, J. M., & Mezzacappa, A. 2006, ApJ, 642, 401
- . 2007, Nature, 445, 58
- Blondin, J. M., Mezzacappa, A., & DeMarino, C. 2003, ApJ, 584, 971
- Blondin, J. M., & Shaw, S. 2007, ApJ, 656, 366
- Bruenn, S. W., et al. 2013, ApJ, 767, L6
- Burrows, A., Dolence, J. C., & Murphy, J. W. 2012, ApJ, 759, 5
- Burrows, A., Hayes, J., & Fryxell, B. A. 1995, ApJ, 450, 830
- Burrows, A., Livne, E., Dessart, L., Ott, C. D., & Murphy, J. W. 2007, ApJ, 655, 416
- Colella, P., & Woodward, P. R. 1984, Journal of Computational Physics, 54, 174
- Couch, S. M. 2013, ApJ, 775, 35
- Couch, S. M., Chatzopoulos, E., Arnett, W. D., & Timmes, F. X. 2015, ApJL, submitted, arXiv:1503.02199
- Couch, S. M., & O’Connor, E. P. 2014, ApJ, 785, 123
- Couch, S. M., & Ott, C. D. 2015, ApJ, 799, 5
- Dolence, J. C., Burrows, A., Murphy, J. W., & Nordhaus, J. 2013, ApJ, 765, 110
- Dubey, A., Antypas, K., Ganapathy, M. K., Reid, L. B., Riley, K., Sheeler, D., Siegel, A., & Weide, K. 2009, J. Par. Comp., 35, 512
- Endeve, E., Cardall, C. Y., Budiardja, R. D., Beck, S. W., Benjood, A., Toedte, R. J., Mezzacappa, A., & Blondin, J. M. 2012, ApJ, 751, 26
- Fernández, R. 2010, ApJ, 725, 1563
- . 2012, ApJ, 749, 142
- Fernández, R., Müller, B., Foglizzo, T., & Janka, H.-T. 2014, MNRAS, 440, 2763
- Fernández, R., & Thompson, C. 2009a, ApJ, 703, 1464
- . 2009b, ApJ, 697, 1827
- Foglizzo, T., Galletti, P., Scheck, L., & Janka, H.-T. 2007, ApJ, 654, 1006
- Foglizzo, T., Masset, F., Guilet, J., & Durand, G. 2012, PRL, 108, 051103
- Foglizzo, T., Scheck, L., & Janka, H.-T. 2006, ApJ, 652, 1436
- Foglizzo, T., et al. 2015, PASA, 32, 9
- Fryer, C. L., & Young, P. A. 2007, ApJ, 659, 1438
- Fryxell, B., et al. 2000, ApJS, 131, 273
- Fryxell, B. A., Müller, E., & Arnett, D. 1989, MPI Astrophys. Rep., 449
- Fuller, J., Cantiello, M., Lecoanet, D., & Quataert, E. 2015, ApJ, submitted, arXiv:1502.07779
- Grefenstette, B. W., et al. 2014, Nature, 506, 339
- Guilet, J., & Fernández, R. 2014, MNRAS, 441, 2782
- Guilet, J., & Foglizzo, T. 2012, MNRAS, 421, 546
- Guilet, J., Sato, J., & Foglizzo, T. 2010, ApJ, 713, 1350
- Handy, T., Plewa, T., & Odrzywotek, A. 2014, ApJ, 783, 125
- Hanke, F., Marek, A., Müller, B., & Janka, H.-T. 2012, ApJ, 755, 138
- Hanke, F., Müller, B., Wongwathanarat, A., Marek, A., & Janka, H.-T. 2013, ApJ, 770, 66
- Herant, M., Benz, W., & Colgate, S. 1992, ApJ, 395, 642
- Hobbs, G., Lorimer, D. R., Lyne, A. G., & Kramer, M. 2005, MNRAS, 360, 974
- Iwakami, W., Kotake, K., Ohnishi, N., Yamada, S., & Sawada, K. 2008, ApJ, 678, 1207
- Iwakami, W., Nagakura, H., & Yamada, S. 2014, ApJ, 786, 118
- Janka, H.-T. 2012, Ann. Rev. Nuc. Part. Sci., 62, 407
- Janka, H.-T., & Müller, E. 1996, A&A, 306, 167
- Kashiyama, K., & Quataert, E. 2015, arXiv:1504.05582
- Kochanek, C. S., Beacom, J. F., Kistler, M. D., Prieto, J. L., Stanek, K. Z., Thompson, T. A., & Yüksel, H. 2008, ApJ, 684, 1336
- Kotake, K., Iwakami-Nakano, W., & Ohnishi, N. 2011, ApJ, 736, 124
- Lattimer, J. M. 2012, Ann. Rev. Nuc. Part. Sci., 62, 485
- Lentz, E. J., Bruenn, S. W., Hix, W. R., Mezzacappa, A., Messer, O. E. B., Endeve, E., Blondin, J. M., Harris, J. A., Marronetti, P., & Yakunin, K. N. 2015, ApJL, in press, arXiv:1505.05110
- Lovegrove, E., & Woosley, S. E. 2013, ApJ, 769, 109
- Lund, T., Marek, A., Lunardini, C., Janka, H.-T., & Raffelt, G. 2010, PRD, 82, 063007
- Lund, T., Wongwathanarat, A., Janka, H.-T., Müller, E., & Raffelt, G. 2012, PRD, 86, 105031
- Marek, A., & Janka, H.-T. 2009, ApJ, 694, 664
- Marek, A., Janka, H.-T., & Müller, E. 2009, A&A, 496, 475
- Melson, T., Janka, H.-T., Bollig, R., Hanke, F., Marek, A., & Mueller, B. 2015a, ApJL, submitted, arXiv:1504.07631
- Melson, T., Janka, H.-T., & Marek, A. 2015b, ApJ, 801, L24
- Mezzacappa, A., et al. 2015, preprint, arXiv:1501.01688
- Müller, B. 2015, MNRAS, submitted, arXiv:1506.05139
- Müller, B., & Janka, H.-T. 2015, MNRAS, 448, 2141
- Müller, B., Janka, H.-T., & Heger, A. 2012, ApJ, 761, 72
- Müller, B., Janka, H.-T., & Marek, A. 2013, ApJ, 766, 43
- Murphy, J. W., & Burrows, A. 2008, ApJ, 688, 1159
- Murphy, J. W., Dolence, J. C., & Burrows, A. 2013, ApJ, 771, 52
- Murphy, J. W., & Meakin, C. 2011, ApJ, 742, 74
- Murphy, J. W., Ott, C. D., & Burrows, A. 2009, ApJ, 707, 1173
- Nadezhin, D. K. 1980, Ap&SS, 69, 115
- Nordhaus, J., Burrows, A., Almgren, A., & Bell, J. 2010, ApJ, 720, 694
- O’Connor, E., & Ott, C. D. 2011, ApJ, 730, 70
- . 2013, ApJ, 762, 126
- Ott, C. D., Burrows, A., Dessart, L., & Livne, E. 2008, ApJ, 685, 1069
- Ott, C. D., et al. 2013, ApJ, 768, 115
- Pejcha, O., & Thompson, T. A. 2012, ApJ, 746, 106
- Piro, A. L. 2013, ApJ, 768, L14
- Porter, D. H., & Woodward, P. R. 1994, ApJS, 93, 309
- Quirk, J. J. 1994, Int. Jour. Num. Meth. Fluids, 18, 555
- Radice, D., Couch, S. M., & Ott, C. D. 2015, Physics of Fluids, submitted, arXiv:1501.03169
- Sana, H., de Mink, S. E., de Koter, A., Langer, N., Evans, C. J., Gieles, M., Gosset, E., Izzard, R. G., Le Bouquin, J.-B., & Schneider, F. R. N. 2012, Science, 337, 444
- Scheck, L., Janka, H.-T., Foglizzo, T., & Kifonidis, K. 2008, A&A, 477, 931
- Sharp, D. H. 1984, Physica D Nonlinear Phenomena, 12, 3
- Smith, N. 2014, ARA&A, 52, 487
- Suwa, Y., Kotake, K., Takiwaki, T., Whitehouse, S. C., Liebendörfer, M., & Sato, K. 2010, PASJ, 62, L49
- Takiwaki, T., Kotake, K., & Suwa, Y. 2012, ApJ, 749, 98

- . 2014, *ApJ*, 786, 83  
Tamborra, I., Hanke, F., Müller, B., Janka, H.-T., & Raffelt, G.  
2013, *PRL*, 111, 121104  
Tamborra, I., Raffelt, G., Hanke, F., Janka, H.-T., & Müller, B.  
2014, *PRD*, 90, 045032  
Thompson, C. 2000, *ApJ*, 534, 915  
Wang, L., & Wheeler, J. C. 2008, *ARA&A*, 46, 433